

Scaling theory for Mott-Hubbard transitions

Anirban Mukherjee, Siddhartha Lal*

Department of Physical Sciences, Indian Institute of Science Education and Research-Kolkata,
Mohanpur, West Bengal 741246, India

*To whom correspondence should be addressed; E-mail: slal@iiserkol.ac.in

A comprehensive understanding of the physics of the Mott insulator has proved elusive due to the absence of any small parameter in the problem. We present a zero-temperature renormalisation group analysis of the one-band Hubbard model in two dimensions at, and away from, half-filling. We find that the transition in the half-filled system involves, for any Hubbard repulsion, passage from a non-Fermi liquid metallic state to a topologically-ordered gapped Mott liquid through a pseudogapped phase bookended by Fermi surface topology-changing Lifshitz transitions. Upon doping, we demonstrate the collapse of the Mott state at a quantum critical point possessing a nodal non-Fermi liquid with superconducting fluctuations, and spin-gapping away from the nodes. d-wave Superconducting order is shown to arise from this critical state of matter. Our findings are in striking agreement with results obtained in the cuprates, offering insight on the origin of superconductivity in strongly correlated quantum matter.

The nature of, and the transition into, the Mott insulating state defines a central problem in strongly correlated quantum matter. An exact solution for the electronic Mott-Hubbard problem

exists only in one spatial dimension [1], while the status of the problem remains open in general. While the Mott insulator is often associated with a ($T = 0$) first order transition leading to a Néel antiferromagnetic ground state [2], the search continues for an insulating state reached via a continuous transition and which breaks no lattice or spin-space symmetries. Indeed, there is some evidence for insulating spin-liquid ground states in layered organic conductors [3] and in Herbertsmithite [4]. Theoretical studies have not, however, identified unambiguously the order parameter for such interaction-driven metal-insulator transitions. These difficulties appear to be associated with an interplay of two complications: the fermion-sign problem limits numerical investigations at low-temperatures [5, 6], while a lack of an identifiable small parameter makes most analytic approaches beyond various mean-field schemes intractable when studying the problem at strong coupling.

Similar issues exist for the case of doped Mott insulators, with the case of the cuprates being most prominent (see [7] for a recent review). While it is by now widely accepted that the physics of the cuprates is associated with that of (almost) decoupled Cu-O layers in which the doped holes (or electrons) pair into a d-wave superconducting state, an overarching understanding of the mechanisms responsible for the observed complex phenomenology remains elusive. Challenges include understanding a non-Fermi liquid (NFL) metallic phase with a striking resistivity that varies linearly with temperature [8], a phase in which parts of the Fermi surface (FS) are gapped (the pseudogap (PG), whose origin and role remain unknown [9]) and the (much debated) existence of a quantum critical point (QCP) within the superconducting dome [10, 11]. That these phases are reached by exiting the Mott insulating state suggest that their origins lie therein [12], highlighting the need for understanding the Mott transition in generality.

Scaling theory for Mott-Hubbard MIT at 1/2-filling. Our analysis adopts the view advocated by Kohn [13]: the FS and its immediate neighbourhood at $T = 0$ are witness to the localisation of electronic states during the passage through the transition. Thus, we implement a scaling

approach where high-energy excitations are integrated out in reaching an effective Hamiltonian for the vicinity of the FS, and their influence appears through renormalised parameters of the theory. Analytic implementations of this approach to the Kondo [14] and Anderson impurity models [15], as well as the superconducting instability of the isotropic FS for the Landau Fermi liquid [16] have revealed how universal states of matter are emergent at low-energies and long-wavelengths from complex microscopic Hamiltonians. Earlier attempts [17, 18] at scaling for the Mott problem have been typically limited to weak- to intermediate-coupling, and have not offered conclusive insight into the physics at stronger couplings.

We analyse the Hubbard model on the two dimensional square lattice at 1/2-filling ($\nu = N_e/2N = 1/2$, N_e : number of electrons, N : number of lattice sites)

$$H = -t \sum_{\langle ij \rangle} (c_i^\dagger c_j + \text{h.c.}) + U \sum_i n_{i\uparrow} n_{i\downarrow}, \quad (1)$$

where the first term denotes electron conduction between nearest neighbours $\langle ij \rangle$ with hopping strength t , and the second an on-site (Hubbard) repulsion $U > 0$. At $\nu = 1/2$ (i.e., one particle per site), it is expected that a critical value $(U/t)_c$ separates a metallic state ($U/t < (U/t)_c$) from an insulating state ($U/t > (U/t)_c$). A notable contrary view is that the insulating state is reached for any $U > 0$ [19, 20]. A resolution of this debate must also offer insight into the nature of the transition, as well as the metallic and insulating states on either side. In developing a scaling approach, we describe the relevant electronic scattering processes away from the FS in terms of Anderson's pseudospin construction (see supplementary materials [21],[22]). As shown in Fig.1(b), these pseudospin electron pairs are placed on high-energy surfaces that are placed parallel to the FS, such that they enjoy the same geometry. Their scattering in the directions along (forward), as well as directly opposite (backward) to, the local normal (\hat{s}) leads to renormalisation of the associated couplings at lower energies and longer lengthscales. We have benchmarked the results obtained from the eventual fixed-point theory at low-energies

against those found from state of the art numerical methods [5] (see Supplementary materials (SM) [21]). Postponing technical details of the RG approach to the Methods section, we present below the major outcomes of the analysis.

Mott MIT at half-filling. The phase diagram obtained, Fig. 1(a), shows the absence of a critical $(U/t)_c$ [19, 20] for the metal-Mott insulator transition for the 1/2-filled Hubbard model on the 2d square lattice. The y-axis of the plot represents an energy scale for quantum fluctuations ($0 < 4 - \omega < 8t$) and the x-axis the bare value of the on-site Hubbard coupling ($0 < U_0 \leq 16 = 2W$) (with the hopping strength $t = 1$). A striking observation is that the transition involves a *pseudogap* phase (PG) arising from a differentiation of electrons based on the monotonic variation of their kinetic energy from node to antinode [24]. This involves a continuous gapping of the FS (Fig.1(e) - 1(h), Video S1) via a steady conversion of poles of the one-particle Greens function into zeros, while respecting the f-sum rule. This is seen within our formalism from the fact that the zeros of the single-particle Greens function are concomitant with the appearance of poles in the two-particle (pseudo)spin Greens function [27, 21]. The PG is initiated in the form of a FS topology changing Lifshitz transition that disconnects the connected FS at the antinodes for $\omega < \omega_{PG} \equiv 0$ (Fig.1(f)), and proceeds until the nodes are gapped via a second Lifshitz transition at $\omega = \omega_{ins}$ (Fig. 1(h)). The transition can, thus, be seen via a topological invariant related to the sign of the (pseudo)spin Greens function: $N_{\hat{s}}(\omega) = e^{i(\pi + \gamma_{\uparrow})}$, $\gamma_{\uparrow} = -i \int_z dz \partial_z \ln(G_{\hat{s},(\uparrow)}(z - \omega))$ (see Methods). For the metal (connected FS), $N_{\hat{s}}(\omega < \omega_{PG}) = 1 \forall \hat{s}$, while for the insulator (gapped FS), $N_{\hat{s}}(\omega > \omega_{ins}) = -1 \forall \hat{s}$. The PG is a coexistence of gapped and gapless parts of the FS, and is characterised by a different topological invariant: $N_{\hat{s}}^{PG} = N_{R\hat{s}} + N_{T\hat{s}}$, where $N_{R/T\hat{s}} = |N_{\hat{s}}(\omega) - N_{\hat{s}+(R/T)\hat{s}}(\omega)|$ and the parity operation $R\hat{s} : \hat{s}_x \leftrightarrow \hat{s}_x, \hat{s}_y \leftrightarrow -\hat{s}_y$ (or vice versa). It is easily seen that $N_{\hat{s}}^{PG} = 1 \forall \hat{s}$ in the PG phase, and vanishes in the metallic and insulating phases. Such non-local order parameters ensure that the two $T = 0$ Lifshitz transitions [21] leading from the metal to the insulator do not belong

to the Ginzburg-Landau-Wilson paradigm [24]. Our results suggest that the nodal-antinodal dichotomy and Fermi arc phenomenology of the doped cuprates [9, 25, 26] originates from the physics at half-filling.

At energies above the entry into the PG ($\omega < \omega_{PG}$), the metal is found to have NFL character in the form of a linear dependence of the resistivity on the quantum energyscale ($\rho(\omega) \sim 4 - \omega$, Fig. 1(c)), vanishing quasiparticle residue [21] as well as a highly broadened electronic spectral function (see, e.g., Fig. 1(d)) possessing an electron lifetime $\tau_{qp} \sim 1/|4 - \omega|$. This ensues from a relevant scaling of the forward scattering coupling, such that collective doublon-holon excitations (encoded in the dynamics of the charge pseudospins) destabilise the Landau quasiparticles and lead to the observed phenomenology of the marginal Fermi liquid [28] (see [21] for further evidence). The Mott insulating ground state reached for $\omega < \omega_{ins}$ is gapped for both charge as well as spin excitations, and possesses the full $SU(2)_{charge} \times SU(2)_{spin}$ symmetry of the parent Hamiltonian. That this liquid-like state possesses topological order can be seen as follows. The spectral gap is created via Umklapp processes associated with a flip of charge pseudospins diametrically across the FS, leading to a net momentum transfer of the center of mass: $\mathbf{P}_{cm} \rightarrow \mathbf{P}_{cm} + 2\pi\hat{Q}_{\pi,\pi}$. This leads to a change in boundary conditions of the center of mass component of the many-body wavefunction [13], gathering a non-zero expectation value for the charge twist operator [29], $\hat{O}_{x,y}^c = \exp[i(2\pi/N) \sum_{\mathbf{r}} \mathbf{r} \cdot (\hat{x}, \hat{y}) \hat{n}_{\mathbf{r}}]$: $\langle \Psi_{CM} | \hat{O}_{x,y}^c | \Psi_{CM} \rangle = e^{i4\pi\nu} \langle \Psi_{CM} | \hat{O}_{x,y}^c | \Psi_{CM} \rangle$, with the filling $\nu = 1/2$. This twist in boundary conditions corresponds to a large gauge transformation on the center of mass degree of freedom by two units of the flux quantum ($\Phi = 2\Phi_0$). $Z^2 \times Z^2$ topological order of the ground state manifold for this Mott liquid placed on a torus is established by the four unique ground states that can be reached by performing a twist in boundary conditions along the x and y directions with only one flux quantum ($\Phi = \Phi_0$): $|\Psi_{CM}, \mathbf{P}_{cm} = 0\rangle, \sqrt{\hat{O}_x^c} |\Psi_{CM}, 0\rangle, \sqrt{\hat{O}_y^c} |\Psi_{CM}, 0\rangle, \sqrt{\hat{O}_x^c \hat{O}_y^c} |\Psi_{CM}, 0\rangle$. These ground states are degenerate in the thermodynamic limit, and the passage between them involves topo-

logical excitations with fractional charge $e\nu \equiv e/2$ close to E_F (see [21]). This can be read from the total phase acquired by the many-body wavefunction from the non-commutativity of the twist operator $\sqrt{O_{x,y}^c}$ and the translation operators along the x and y-directions ($T_{x,y}$) : $T_{x/y}\sqrt{O_{x/y}^c} = e^{i2\pi\nu}\sqrt{O_{x/y}^c}T_{x/y}$, $\nu = 1/2$ and an exchange statistical angle $\theta = \pi\nu = \pi/2$ [30]. It is well understood that such ground states possess short-ranged resonating valence bond (RVB) order [12, 31, 11]. Further, our RG analysis shows that this topologically ordered Mott liquid ground state is replaced by a (π, π) charge density wave (CDW) broken symmetry ground state in the presence of a staggered chemical potential. Similar arguments establish the existence of topological order in the spin sector of the Mott liquid, and symmetry breaking to a (π, π) spin density wave (SDW) Néel ground state via a staggered magnetic field [21].

Mottness Collapse and quantum criticality with doping. We present the RG phase diagram for the 2D Hubbard model with doping away from 1/2-filling in Fig.2(a). This phase diagram results from the inclusion of effects of doping and tangential scattering processes across the Fermi surface. The primary effect of doping is in providing separate quantum energyscales for the pseudogapping effects of spin and charge fluctuations: while spin fluctuations start gapping the antinodes at $\omega > \omega_{PG} \equiv \omega_{PG}^s$ for all doping, initiation of the pseudogapping of charge fluctuations (ω_{PG}^c) falls linearly with increasing doping: $\omega_{PG}^c = -\mu_{eff}$, where the effective chemical potential with doping is tuned via a Hartree-shift arising from the bare Hubbard coupling, $\mu_{eff} = -U_0/2$. This tuning of the chemical potential immediately lowers the $SU(2)_{charge}$ symmetry of the 1/2-filled system to $U(1)_{charge}$ by explicitly breaking the particle-hole symmetry in the doublon-holon sector [32]. The collapse of Mottness [33, 34] ends at a QCP at $\omega_{PG}^{c*} = W/2 = -\mu_{eff}^*$ with a point-like Fermi surface at the nodes and spin-gapping which increases monotonically from the nodes to the antinodes (Fig.2(d), Videos S2, S3). Importantly, the QCP possesses emergent chiral $(SU(2)_{charge} \times SU(2)_{spin})_{R/L}$ symmetries. Recall that similar symmetries exist for the particle-hole symmetric 1/2-filled Hubbard model. Indeed, these

findings for the QCP are in striking agreement with the works of Phillips and co-workers [35]. For $\omega > \omega_{PG}^{c*}$, at low energies and to the left of the QCP lies the Mott liquid (Fig.2(f), Video S4) discussed earlier. For $\omega > \omega^t = \mu_{eff} - 2\mu_{eff}^*$, to the right of the QCP lies a correlated Fermi liquid (CFL) arising from RG relevant tangential scattering (Fig.2(f)). The CFL is associated with well-defined electronic quasiparticles coexisting with NFL metal on different stretches of a connected FS [21]. These findings are consistent with results obtained from the dynamical cluster quantum Monte Carlo method applied to the 2D Hubbard model with doping away from 1/2-filling [36], and unveil the mechanism responsible for the experimentally observed topological reconstruction of the Fermi surface near critical doping [25, 26, 37].

At the QCP, while tangential scattering is irrelevant everywhere on the FS, Umklapp and spin backscattering are RG relevant everywhere *but at the nodes* [21]. This is a topological protection of the nodal degrees of freedom, arising from the phase of the charge pseudospin Greens function being $\gamma_{\uparrow}(\text{node}, \omega_{PG}^{c*}) = 2\pi$ (in the doublon basis), leading to a sign $N_{\text{node}}(\omega_{PG}^{c*}) = -1$. The relevant charge and spin forward scattering couplings lead, instead, to a spin-pseudogapped NFL metallic state along the nodal directions (Fig.1(b),(c)), extending to finite energyscales in the wedge-like quantum critical region directly above the QCP ($\omega < \min(\omega_{PG}^{c*}, \omega^t)$, Fig.2(a),(e)), merging finally into the NFL with a connected FS at very high energies [28]. Such a nodal liquid state appears to have been observed in ARPES measurements carried out within the PG phase of the slightly underdoped cuprate Bi2212 above the superconducting dome [38]. In addition, this spin-gapped metallic state possesses large pairing fluctuations with d-wave symmetry [39]. Our finding of pairing fluctuations prior to the onset of superconducting off-diagonal long-range order is in agreement with the findings from Nernst experiments on various members of the cuprates [40]. Below, these fluctuations will be seen to interplay with the spin-gap in leading to d-wave superconductivity [41].

Symmetry breaking and superconductivity. The full RG phase diagram away from 1/2-filling

and with (π, π) CDW, (π, π) SDW and d-wave superconducting broken symmetry orders is shown in Fig.3. We find the (π, π) SDW for energies $\omega \geq \omega_{ins} = 2.8$ and doping $0 > \mu_{eff} \geq -1.75$, and the (π, π) CDW for energies $\omega \geq 3.2$ and doping $-3.05 \geq \mu_{eff} \geq -4$. A d-wave superconducting dome is found to extend between a doping range of $-1.5 \geq \mu_{eff} \geq -6$ and has an optimal gap scale (Δ_{SC}) at the critical doping $\mu_{eff} = -4$ corresponding to the QCP. The optimal quantum fluctuation energy scale for the onset of superconductivity is the kinetic energy of a pair of electrons from diametrically opposite nodal points on the FS: $W/2 - \omega_{SC} = W/2 - 2\epsilon_{\Lambda^* \hat{s}_{node}}$, where Λ^*/Λ_0 is the dimensionless spectral weight for the marginal nodal electronic quasiparticles obtained from the RG. Deep in the underdoped regime ($-1.5 \geq \mu_{eff} \geq -1.75$), a coexistence of the SDW and d-wave superconducting orders appears likely (Fig. 4(a)). The suppression of d-wave superconductivity is clearly observed in the presence of the CDW order (Fig.4(b)); the charge-gap dominated Mott liquid (dark blue region in Fig.(3)) leads to further suppression of superconductivity. These results obtained are in consonance with the finding of two distinct antinodal energy-gap scales in recent ARPES and STM experiments carried out on the PG phase of the cuprate La-Bi2201 [42], one of which appears to be linked with the onset of superconductivity and the other with charge ordering. For $-4 \geq \mu_{eff} \geq -6$, the competition between the nodal NFL metal, the spin-pseudogapped parts of the FS and the tangential scattering leads to the reconstruction of the FS [21]. This is apparent in the suppression of superconducting fluctuations (dashed line in Fig.3) beyond critical doping and shows how competition with the CFL suppresses d-wave superconductivity. Variations of the resistivity (ρ) and inverse superfluid stiffness (σ_{SC}^{-1}) upon tuning ω towards the QCP and the CFL are shown Fig.4(c) and Fig.4(d) respectively (see also Videos S5, S6). Maps of the single-particle spectral function $A(E)$ within and in the neighbourhood of the d-wave SC phase are also presented in Fig.4(e)-(h). These results are in broad agreement with several transport and spectroscopy measurements made in various parts of the cuprates phase diagram

[7, 9, 10, 25, 26, 37, 38, 40, 42].

We now establish the origin of the d-wave superconducting order as the QCP at $\mu_{eff}^* = -4$. We have shown above the the nodal points support a gapless NFL metal, as the irrelevance of all gapping mechanisms at the nodes arise from the topological signature of the doublon propagator. Thus, the onset of superconductivity at critical doping [21] takes place in the backdrop of this protection for the nodal gapless states. We have also seen that the spin-gap at critical doping has d-wave structure, but without a sign change across the nodes. A $U(1)$ symmetric breaking RG calculation [21] further reveals that the nodal points act as domain walls for the growth of the superconducting order upon scaling down to low energies: the RG-integrated superconducting order parameter $\langle c_{\Lambda-T\hat{s}\downarrow}^\dagger c_{\Lambda\hat{s}\uparrow}^\dagger \rangle = -\langle c_{\Lambda-\hat{s}\downarrow}^\dagger c_{\Lambda T\hat{s}\uparrow}^\dagger \rangle \propto e^{i\gamma_{\hat{s},\hat{s}_{node}}}$, where the relative phase $\gamma_{\hat{s},\hat{s}_{node}} = -i \ln(\text{sgn}[2(\epsilon_{\Lambda\hat{s}} - \epsilon_{\Lambda\hat{s}_{node}})])$ and $2(\epsilon_{\Lambda\hat{s}} - \epsilon_{\Lambda\hat{s}_{node}})$ is the energy scale for a Cooper pair (with respect to the nodes). The alternation of sign in this energy scale is, thus, the alternation in sign of the pairing order paramter.

Conclusions. We conclude with a few striking consequences of our analysis. First, even as the d-wave superconducting phase shields its origin from a QCP lying at critical doping, it possesses properties of that criticality (e.g., gapless nodes, gap with d-wave symmetry). Second, the QCP involves a drastic change in the nature of the ground state and low-lying excitations: from fractionally charged excitations (gapped Mott liquid at underdoping) to electronic quasi-particles (CFL at overdoping) through critical fermionic collective excitations emergent at the QCP (nodal NFL at critical doping). The associated change in the exchange statistics of the excitations has been called *statistical quantum criticality* [34]. Third, the qualitative agreement of RG phase diagram, Fig.3, with the experimentally obtained temperature versus doping phase diagram for the cuprates [7] is remarkable. This settles conclusively a long-standing debate on whether the physics of the one-band Hubbard model at and away from 1/2-filling is pertinent to the physics of high-temperature superconductivity [43]. Our results are likely pertinent to the

ubiquitous presence of superconductivity in several other forms of strongly correlated quantum matter, e.g., the heavy-fermion systems [44]. Finally, our formalism predicts that the kinetic energy of nodal fermions is related to the optimal quantum fluctuation energy scale for the onset of d-wave superconducting order: depressing the former (e.g., by tuning the curvature of the Fermi surface via next-nearest neighbour hopping [45]) should enhance the latter.

References

- [1] E. H. Lieb, F. Y. Wu, *Phys. Rev. Lett.* **20**, 1445 (1968).
- [2] M. Imada, *et al. Rev. Mod. Phys.* **70**, 1039 (1998).
- [3] Y. Kurosaki, *et al. Phys. Rev. Lett.* **95**, 177001 (2005).
- [4] J. Helton, *et al., Phys. Rev. Lett.* **104**, 147201 (2010).
- [5] J. LeBlanc, *et al., Phys. Rev. X* **5**, 041041 (2015).
- [6] M. Iazzi, *et al. Phys. Rev. B* **93**, 115102 (2016).
- [7] B. Keimer, *et al. Nature* **518**, 179 (2015).
- [8] S. Martin, *et al. Phys. Rev. B* **41**, 846 (1990).
- [9] U. Chatterjee, *et al., PNAS* **108**, 9346 (2011).
- [10] J. Tallon, J. Loram, *Physica C* **349**, 53 (2001).
- [11] S. Sachdev, *Rev. Mod. Phys.* **75**, 913 (2003).
- [12] P. W. Anderson, *Science* **235**, 1196 (1987).
- [13] W. Kohn, *Phys. Rev.* **133**, A171 (1964).

- [14] P. Anderson, *J. Phys. C: Sol. St. Phys.* **3**, 2436 (1970).
- [15] F. Haldane, *Phys. Rev. Lett.* **40**, 416 (1978).
- [16] R. Shankar, *Rev. Mod. Phys.* **66**, 129 (1994).
- [17] W. Metzner, *et al. Rev. Mod. Phys.* **84**, 299 (2012).
- [18] S. Raghu, *et al. Phys. Rev. B.* **81**, 224505 (2010).
- [19] P. W. Anderson, *Adv. Phys.* **46**, 3 (1997).
- [20] S. Moukouri, M. Jarrell, *Phys. Rev. Lett.* **87**, 167010 (2001).
- [21] Please refer to Supplementary Materials.
- [22] P. W. Anderson, *Phys. Rev.* **112**, 1900 (1958).
- [23] G. E. Volovik, *The universe in a helium droplet* (Oxford University Press, 2009).
- [24] M. Imada, *et al. J. Phys.: Cond. Matt.* **22**, 164206 (2010).
- [25] Y. He, *et al. Science* **344**, 608 (2014).
- [26] K. Fujita, *et al. Science* **344**, 612 (2014).
- [27] R. M. Martin, *Phys. Rev. Lett.* **48**, 362 (1982).
- [28] C. M. Varma, *et al. Phys. Rev. Lett.* **63**, 1996 (1989).
- [29] M. Oshikawa, *Phys. Rev. Lett.* **84**, 1535 (2000).
- [30] M. Oshikawa, T. Senthil, *Phys. Rev. Lett.* **96**, 060601 (2006).
- [31] E. Fradkin, *Field theories of condensed matter physics* (Cambridge University Press, 2013).

- [32] H. R. Krishnamurthy, *et al. Phys. Rev. Lett.* **64**, 950 (1990).
- [33] P. Phillips, *Phil. Trans. Roy. Soc. Lond. A* **369**, 1574 (2011).
- [34] J. Zaanen, B. Overbosch, *Phil. Trans. Roy. Soc. Lond. A* **369**, 1599 (2011).
- [35] S. Chakraborty, *et al. Phys. Rev. B* **82**, 214503 (2010).
- [36] N. S. Vidhyadhiraja, *et al. Phys. Rev. Lett.* **102**, 206407 (2009).
- [37] F. F. Balakirev, *et al., Nature* **424**, 912 (2003).
- [38] A. Kanigel, *et al., Nat. Phys.* **2**, 447 (2006).
- [39] V. Emery, S. Kivelson, *Nature* **374**, 434 (1995).
- [40] Y. Wang, *et al. Phys. Rev. B* **73**, 024510 (2006).
- [41] S.-X. Yang, *et al., Phys. Rev. Lett.* **106**, 047004 (2011).
- [42] J.-H. Ma, *et al., Phys. Rev. Lett.* **101**, 207002 (2008).
- [43] F. C. Zhang, T. M. Rice, *Phys. Rev. B* **37**, 3759 (1988).
- [44] C. Pépin, *Phys. Rev. B* **77**, 245129 (2008).
- [45] E. Pavarini, *et al. Phys. Rev. Lett.* **87**, 047003 (2001).
- [46] S. D. Glazek, K. G. Wilson, *Phys. Rev. B* **69**, 094304 (2004).
- [47] L. N. Cooper, *Phys. Rev.* **104**, 1189 (1956).
- [48] H. Kleinert, *Path integrals in quantum mechanics, statistics, polymer physics, and financial markets*, World Scientific, Singapore (2006).

- [49] J. Zaanen, *et al. Iranian J. Phys. Res.* **8**, 39 (2008).
- [50] D. K. Hong, S. D. H. Hsu, *Phys. Rev. D* **66**, 071501 (2002).
- [51] M. Alford, A. Kryjevski, *Journal of Physics G* **37**, 025002 (2010).
- [52] J. Zaanen, *Science* **319**, 1205 (2008).
- [53] A. A. Abrikosov, L. P. Gorkov and I. E. Dzyaloshinski, *Methods of Quantum Field Theory in Statistical Physics*, Prentice Hall, New Jersey (1963), pgs.85-93.
- [54] A. E. Ruckenstein and S. Schmitt-Rink, *Int. J. Mod. Phys. B.* **3**, 1809 (1989).
- [55] J. S. Langer and V. Ambegaokar, *Phys. Rev.* **121**, 1090 (1961).
- [56] J. M Luttinger, *Phys. Rev.* **119**, 1153 (1960).
- [57] N. Iqbal, H .Liu, M. Mezei, *JHEP* **1204**, 086 (2012).
- [58] J. Zaanen, Y.-W. Sun, Y. Liu and K. Schalm, *Holographic duality in condensed matter physics* (Cambridge University Prese, 2015), pgs.99, 270.

Acknowledgments

The authors thank R. K. Singh, A. Taraphder, S. Sinha, M. S. Laad, G. Baskaran, A. M. Srivastava, B. Bansal, S. Raj, P. Majumdar, S. Pal and S. Patra for several discussions and feedback. A. M. thanks the CSIR, Govt. of India for funding through a junior and senior research fellowship. S. L. thanks the DST, Govt. of India for funding through a Ramanujan Fellowship (2010-2015) during which a part of this work was carried out. The authors declare that they have no competing interests.

Methods

The leading scattering processes in the neighbourhood of the Fermi surface can be written in

terms of Anderson pseudospin operators constructed from electron-electron and electron-hole spinors respectively [22] placed at an off-set Λ for every direction normal to the Fermi surface (FS) \hat{s} (see Supplementary Fig.S1)

$$\begin{aligned} \left| \Psi_{\hat{s},\Lambda}^{c,s}, \pm \frac{1}{2} \right\rangle &= \left| f_{\Lambda\hat{s}}^{c,s;\dagger} \hat{\sigma} f_{\Lambda\hat{s}}^{c,s} = \pm \frac{1}{2} \right\rangle, \\ f_{\Lambda\hat{s}}^{c\dagger} &= \left[c_{\Lambda,\sigma}^\dagger(\hat{s}) c_{-\Lambda,-\sigma}(T\hat{s}) \right], \quad f_{\Lambda\hat{s}}^{s\dagger} = \left[c_{\Lambda,\sigma}^\dagger(\hat{s}) c_{-\Lambda,-\sigma}^\dagger(T\hat{s}) \right]. \end{aligned} \quad (2)$$

This yields a two-particle spin-charge hybridised pseudospin Greens function

$$G_{\hat{s},(\downarrow,\uparrow)}^{-1}(\omega, \Lambda) = (e^{i\gamma_{\downarrow,\uparrow}(\hat{s},\omega)}/2) |\omega - p\epsilon_{\Lambda\hat{s}}^c - (1-p)\epsilon_{\Lambda\hat{s}}^s|, \quad (3)$$

where the dispersions for the Anderson pseudospins for charge and spin excitations are $\epsilon_{\Lambda\hat{s}}^{c,s} = \epsilon_{\Lambda\hat{s}} \pm \epsilon_{-\Lambda T\hat{s}}$ ($T\hat{s} : \hat{s}_x \leftrightarrow \hat{s}_y$) and the phases $\gamma_{\downarrow,\uparrow}(\hat{s}, \omega)$ signify the signature of $G_{\hat{s},(\downarrow,\uparrow)}$ [23]

$$\gamma_{\downarrow,\uparrow}(\hat{s}, \omega) = -i \int_z dz \partial_z Tr_{\downarrow,\uparrow} \ln(G_{\hat{s},(\downarrow,\uparrow)}(z - \omega, \Lambda)). \quad (4)$$

The renormalisation group procedure is formulated via a recursive Gauss-Jordan folding of pseudospin states along every \hat{s} starting from energies far away from, and approaching, the FS. As is common with all RG schemes, this yields a renormalisation of all couplings associated with various scattering processes. From these couplings, we construct a low-energy stable fixed point theory. (See Supplementary Materials [21] for a detailed discussion)

The RG equations obtained, for instance, for the forward ($V_{\mathbf{Q}_{\eta\eta'}=(0),\hat{s}}^{c,s}$) and backward scattering ($V_{\mathbf{Q}_{\eta\eta'}=(\pi),\hat{s}}^{c,s}$) couplings for charge pseudospin (c) and spin (s) excitations for every direction normal to the FS (\hat{s}) are

$$\frac{\Delta V_{\mathbf{Q}_{\eta\eta'}=(0,\pi),\hat{s}}^{c,s}}{\Delta \log(\Lambda/\Lambda_0)} = \frac{p_{c,s} (V_{\mathbf{Q}_{\eta\eta'},\hat{s}}^{c,s})^2}{e^{i\gamma_{\downarrow,\uparrow}^{\downarrow,\uparrow}} |G_{\hat{s},(\downarrow,\uparrow)}^{-1}(\omega, \Lambda)| - p_c \frac{V_{\mathbf{Q}_{\eta\eta'},\hat{s},n}^c}{4} - p_s \frac{V_{\mathbf{Q}_{\eta\eta'},\hat{s}}^s}{4}}. \quad (5)$$

The RG equations have been cast as difference equations to take account of the non-linear dispersion and discrete nature of the electronic Hilbert space. The couplings $\Delta V_{\mathbf{Q}_{\eta\eta'}=(0,\pi),\hat{s}}^{c,s}$

represent, as always, changes in the bare values with changes in the logarithmic dimensionless energyscale $\Delta \log(\Lambda/\Lambda_0)$ as the discrete scaling transformations are carried out. Here η and η' denote positions of a (pseudo)spin electron pair (\uparrow, \downarrow) with respect to the FS before and after a scattering event, such that $Q_{\eta\eta'}$ gives a scattering wavevector for forward scattering ($\eta = \eta'$, $Q = 0$) and backward scattering ($\eta' = -\eta$, $Q = \pi$). The logarithmic dimensionless scale ($\log(\Lambda/\Lambda_0)$) denotes the distance from the FS in energy-momentum space. The RG equations are solved numerically in an iterative manner on a two-dimensional grid in momentum-space, obtaining a phase diagram as well as several physical observables from fixed point values of various couplings, spectral weights and gaps [21].

List of Supplementary Materials

Supplementary Text

Figures S1 - S12

Figure Captions

Fig.1: Passage through Mott MIT. (a) Renormalisation group phase diagram for the 1/2 filled Hubbard model in the quantum fluctuation energyscale $(4 - \omega)$ -bare repulsion (U_0) plane. Colourbar represents many-body gap (Δ) averaged around erstwhile Fermi surface(FS). Transition from non-Fermi liquid (NFL, white) to Mott liquid (ML, dark blue) insulator is through a pseudogap (PG, shaded blue) for all $U_0 > 0$. ω_{PG} and ω_{ins} are energy scales for Lifshitz transitions that initiate and end the PG respectively. (b) Schematic representation of shells (black lines parallel to and formed around the FS (red line) with spacing Λ) of states that are integrated out from first quadrant of Brillouin zone (BZ): $0 < k_x, k_y < \pi$. Inset (top right): Umklapp scattering of electron pairs. Inset (bottom left): variation in density of states from antinode (AN) to node (N). The pair of black dots represents electron pair pseudospin for charge/spin excitations in the up orientation formed around the node (cyan dot); white dots represents the opposite

orientation. \hat{s} represents the direction normal to FS. (c)-(h) obtained for $U_0 = 8$. (c) Linear variation of resistivity (ρ) with $\omega < \omega_{PG}$ in NFL crosses over through PG ($\omega_{PG} < \omega < \omega_{ins}$) into the ML (diverging ρ for $\omega > \omega_{ins}$). (d) Quasiparticle (qp) spectral function ($A(E)$) for $\omega = 2.5$, showing NFL at N and gap at AN and averaged over FS (A_{total}). (e-h) Map of progression of $A(E)$ (colourbar:red to yellow) and Δ (colourbar:cyan to violet) in first quadrant of BZ with changing ω . (e) shows connected Fermi surface with broadened $A(E)$ of NFL ($\omega = -0.1$) on brink of first Lifshitz transtion at AN (f, $\omega = 0.1$). (g) shows FS arc in PG ($\omega = 2.5$) leading to final gapping of N at second Lifshitz transition ($\omega = 2.8$).

Fig.2: Quantum criticality from the collapse of Motttness. (a) RG phase diagram for 2D Hubbard model with hole doping showing quantum critical point (QCP) at $-\mu_{eff} = 4 = \omega$ and its wedge extending to higher energies. All phases (NFL, PG, ML, correlated Fermi liquid (CFL), PG-CFL and QCP-wedge) and related energy scales are shown in the colour bars, and discussed in detail in the text. Dashed line shows highest energy scale for superconducting fluctuations. Insets: N, AN and FS-averaged $A(E)$ for the PG-CFL (misty-grey region: $\omega = 3.2, \mu_{eff} = -5.5$) and gapless CFL (grey region: $\omega = 3.2, \mu_{eff} = -7.5$). (b) Resistivity (ρ) vs. $4 - \omega$ for various μ_{eff} , showing passage from NFL into (blue) ML, (green) the QCP and (red) PG-CFL. (c) N, AN and FS-averaged $A(E)$ at the QCP. (d)-(g) Maps of $A(E)$ in the neighbourhood of the QCP (see (a)). (d): at QCP (nodal spin-PG NFL), (e): vertically above QCP (spin-PG Fermi arc NFL), (f): to left (ML), (g): to right (CFL).

Fig.3: Symmetry broken orders with doping. RG phase diagram for 2D Hubbard model with doping and (π, π) CDW (green), (π, π) SDW (red) and d-wave Superconducting (SC) orders (yellow) included. Gap scales and spectral weights for various phases are shown in the colour bars. Origin of superconductivity from spin-PG nodal NFL with superconducting fluctuations is described in text. The SC “dome” is centered about the QCP (optimality) and falls away on either side due to competition with insulating orders (underdoped) and gapless CFL

(overdoped).

Fig.4: Passage through the Phase diagram away from 1/2-filling. (a)-(d) Resistivity (ρ) with (green) and without any form of symmetry-breaking (blue), and inverse superfluid stiffness (σ_{SC}^{-1} , yellow) at various dopings. (a) $\mu_0 = -1.75$: passage from PG to ML (blue), from PG to SC through spin-gap dominated ML. Inset: Peak in spin susceptibility within SC region. (b) $\mu_0 = -3.25$: passage from PG to ML (blue), from PG to SC through charge-gap dominated ML. Inset: Peak in charge susceptibility within SC region. (c) $\mu_0 = -4$: passage from NFL with connected FS to spin-PG nodal NFL at QCP (blue), from NFL to SC through spin-PG nodal NFL (green). (d) $\mu_0 = -5.5$: passage from NFL to PG-CFL (blue), from NFL to SC through PG-CFL (green). (e)-(h) Maps of $A(E)$ around the SC dome (see Fig.(3)), black curves show extent of SC fluctuations around FS. (e): vertically above dome at optimal doping, colours as in Fig. (2(e)). (f): to left of dome (ML). (g): within d-wave SC dome, with nodal NFL. (h): to right of dome (CFL).

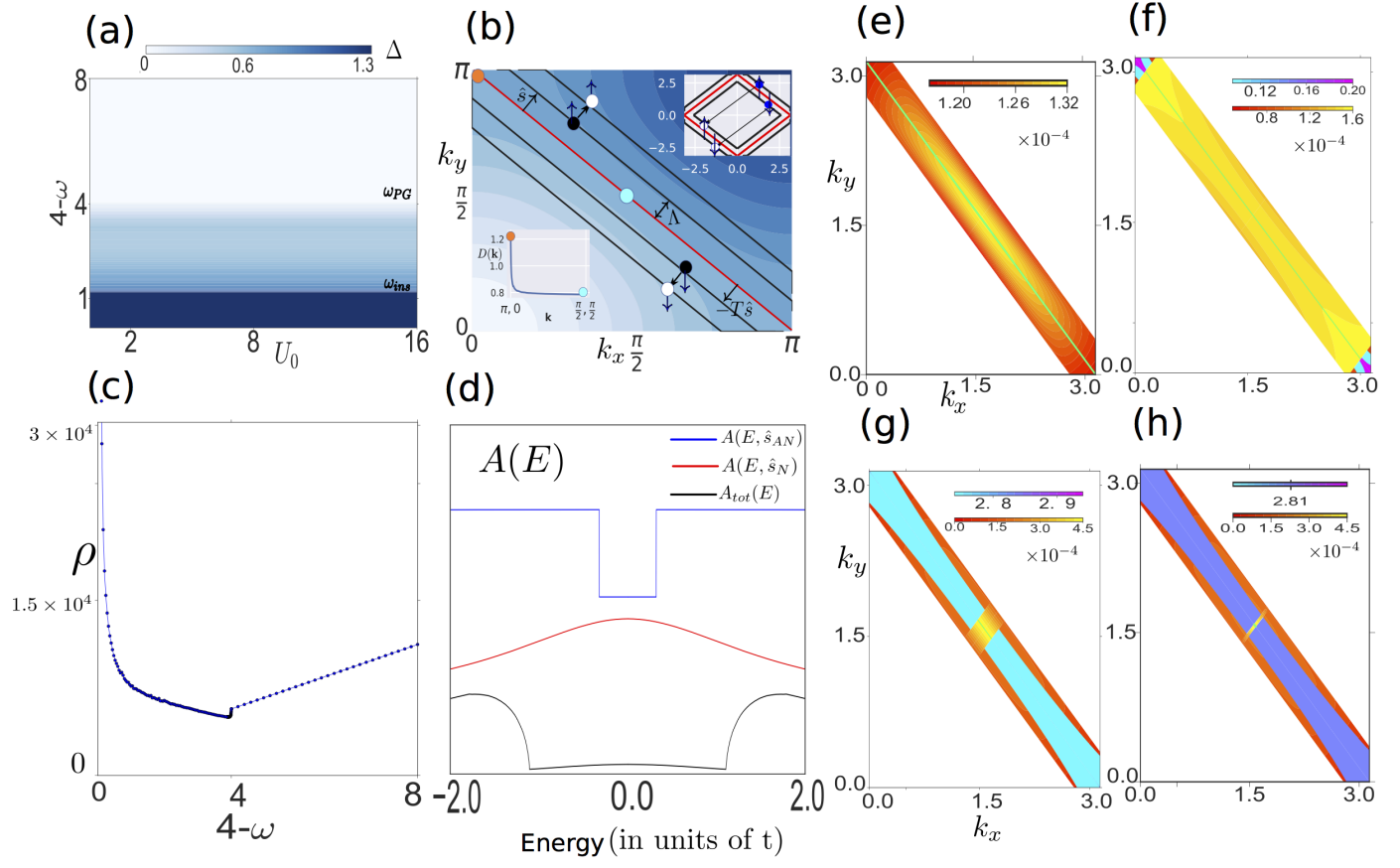


Figure 1

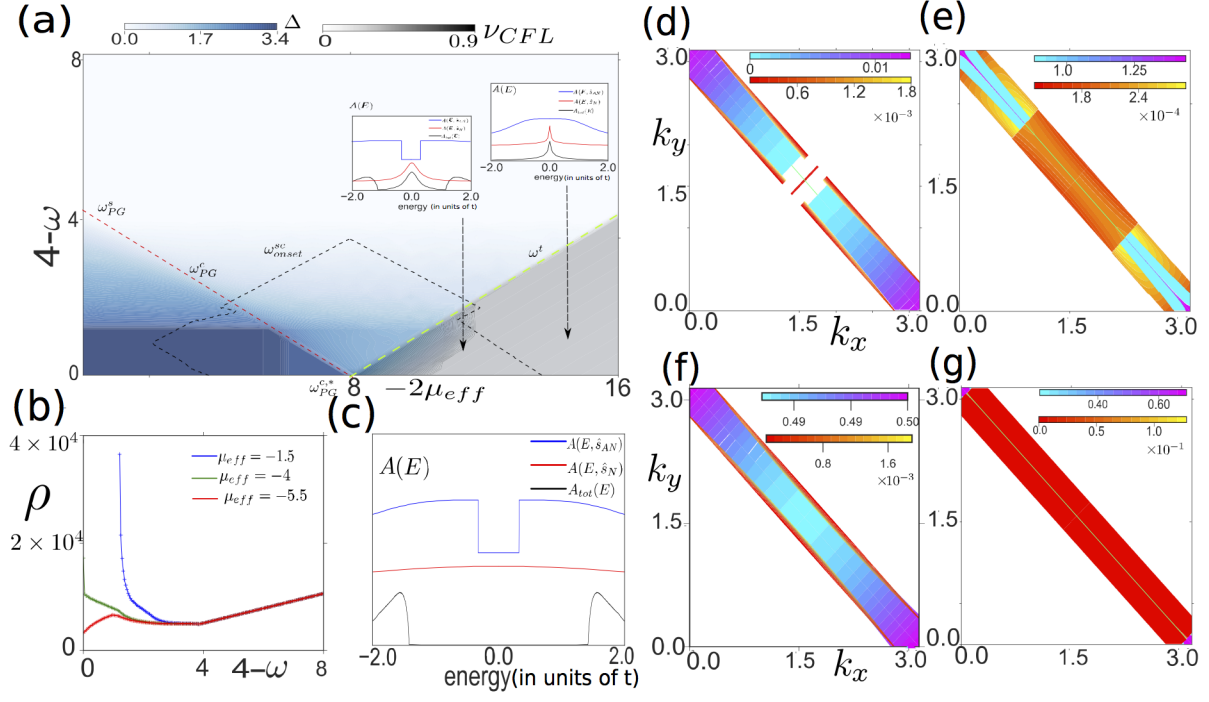


Figure 2

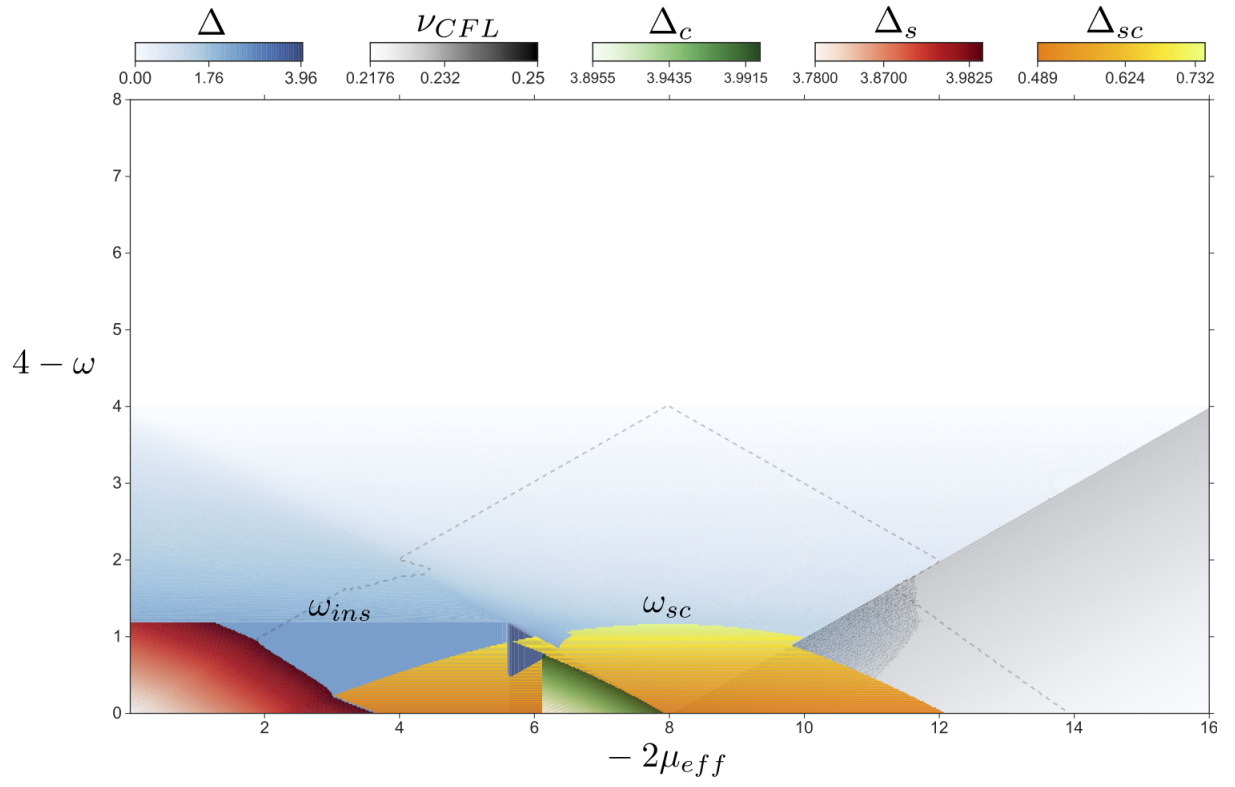


Figure 3

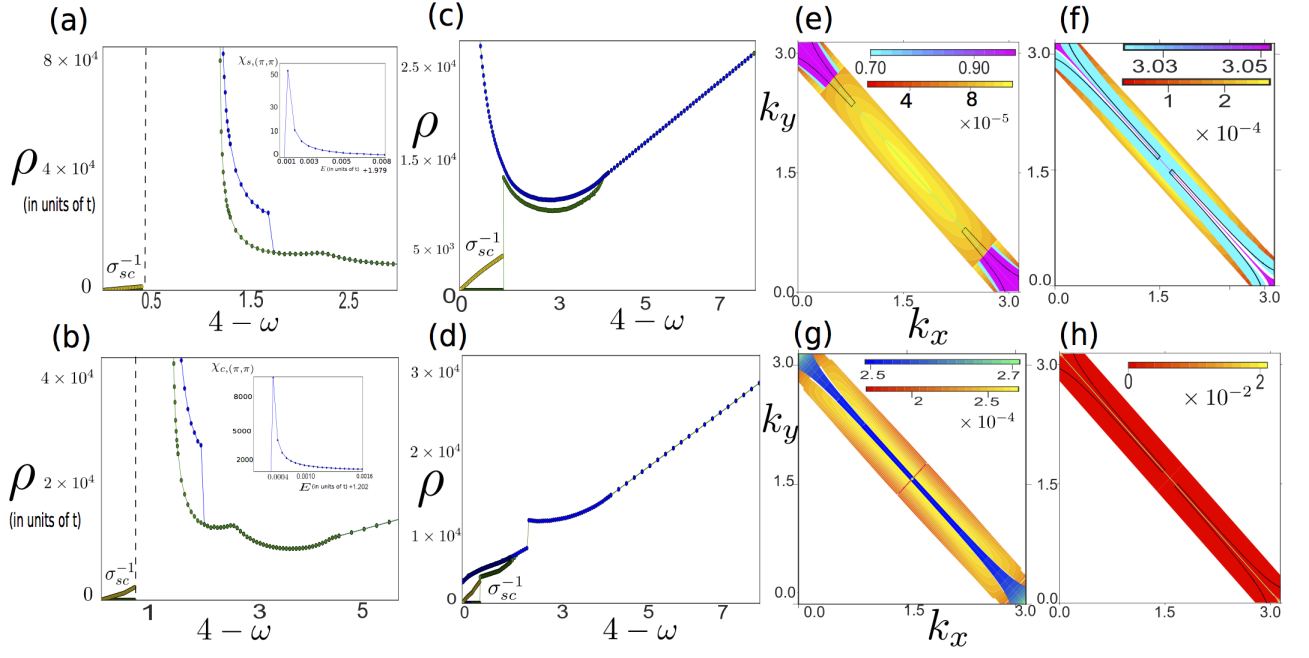


Figure 4:

Supplementary Materials for Scaling theory for Mott-Hubbard transitions

Authors: Anirban Mukherjee, Siddhartha Lal

Department of Physical Sciences, Indian Institute of Science Education and Research-Kolkata,
Mohanpur, West Bengal 741246, India

Supplementary Text. The supporting arguments and evidence provided here have been divided into several parts. Section 1 involves the schematics and technical details of the non-perturbative renormalization group (RG) approach adopted by us and its implications, while section 2 presents detailed results from the RG. Section 3 presents additional results on several properties of the various phases in the phase diagrams for the 2D Hubbard model on the square lattice at, and away from, 1/2-filling. Section 4 presents a detailed derivation of the renormalised single particle Greens function, and section 5 presents the demonstration of the f-sum towards understanding dynamical spectral weight redistribution.

1 Schematics of the Renormalization Group

We analyze the 2d-Hubbard model with doping described by,

$$\hat{H} = \sum_{\mathbf{k}, \sigma} (\epsilon_{0\mathbf{k}} - \mu_{eff}) c_{\mathbf{k}\sigma}^\dagger c_{\mathbf{k}\sigma} + U_0 \sum_{\mathbf{r}} \left(\hat{n}_{\mathbf{r}\uparrow} - \frac{1}{2} \right) \left(\hat{n}_{\mathbf{r}\downarrow} - \frac{1}{2} \right), \quad (6)$$

where $c_{\mathbf{k}\sigma}^\dagger/c_{\mathbf{k}\sigma}$ is the electron creation/annihilation operator with wave-vector \mathbf{k} and spin σ , $\hat{n}_{\mathbf{r}\sigma} = c_{\mathbf{r}\sigma}^\dagger c_{\mathbf{r}\sigma}$ is the number operator at lattice site $\mathbf{r} = j_1 \hat{x} + j_2 \hat{y}$, and the bare dispersion is given by $\epsilon_{0\mathbf{k}} = -2t(\cos k_x + \cos k_y)$, with t_1 being the nearest neighbour hopping strength, U_0 is the strength of on-site interaction, $\mu_{eff} = \mu - \frac{U_0}{2}$. In the presence of two-particle interactions states in the neighbourhood the Fermi surface get populated virtually even at $T = 0K$ due to quantum mechanical two particle scattering processes. In order to understand the effects of such low energy fluctuations in the neighbourhood of the Fermi surface generated via such scattering

processes we develop a family of shells around the Fermi surface imbibing its geometry. On such shells off-setted from the Fermi energy we develop a scaling approach to understand the effect of fluctuations for the low energy region.

1.1 Construction of curves off-setted parallel to the Fermi surface(FS)

We define a window of width $2|\Lambda_0|$ around the Fermi surface FS by drawing lower and upper parallel(offset) curves around it. FS is constituted by family of wave-vectors $F := \{\mathbf{k}_F, s.t. \epsilon_{0\mathbf{k}_F} = \mu_{eff}\}$. The unit vectors along Fermi surface velocities $\mathbf{v}_F = \nabla \epsilon_{0\mathbf{k}}|_{\mathbf{k}=\mathbf{k}_F}$ form $\mathcal{N}_F := \{\hat{\mathbf{s}} = \mathbf{v}_F/|\mathbf{v}_F|, \mathbf{k}_F \in F\}$. The offset curves $C_{F,\Lambda}$'s are defined as normal translations of the Fermi surface wave-vectors $\mathbf{k}_\Lambda(\hat{\mathbf{s}}) = \mathbf{k}_F(\hat{\mathbf{s}}) + \Lambda\hat{\mathbf{s}}$, The fermionic creation/annihilation operators along $C_{F,\Lambda}$ can be represented compactly as $c_{\mathbf{k}_\Lambda(\hat{\mathbf{s}}),\sigma}^\dagger = c_{\Lambda,\sigma}^\dagger(\hat{\mathbf{s}}), c_{\mathbf{k}_\Lambda(\hat{\mathbf{s}}),\sigma} = c_{\Lambda,\sigma}(\hat{\mathbf{s}})$.

Pseudospin construction on offset curves: In order to take account of four fermionic longitudinal (forward and backward scattering) and tangential scattering terms we define a pseudo-spin basis for pair of electronic states about the nodal wave-vector around the neighbourhood of FS [22],

$$|\Psi_{\hat{\mathbf{s}},\Lambda_n,\uparrow,\downarrow}\rangle = \sqrt{q_l}|\Psi_{\hat{\mathbf{s}},\Lambda_n}^p, \pm\frac{1}{2}\rangle + \sqrt{q_t}|N_{\Lambda_n}^r, \pm\frac{1}{2}\rangle, \quad (7)$$

where ,

$$|\Psi_{\hat{\mathbf{s}},\Lambda_n}^p, \pm\frac{1}{2}\rangle = \sqrt{p_c}|\Psi_{\hat{\mathbf{s}},\Lambda_n}^c, \pm\frac{1}{2}\rangle + \sqrt{p_s}|\Psi_{\hat{\mathbf{s}},\Lambda_n}^s, \pm\frac{1}{2}\rangle, \quad |N_{\Lambda_n}^r, \pm\frac{1}{2}\rangle = \sqrt{r_c}|N_{\Lambda_n}, \pm\frac{1}{2}\rangle_c + \sqrt{r_s}|N_{\Lambda_n}, \pm\frac{1}{2}\rangle_s, \quad (8)$$

and ,

$$\begin{aligned} \left| \Psi_{\hat{\mathbf{s}},\Lambda_n}^{c,s}, \pm\frac{1}{2} \right\rangle &= \left| f_{\Lambda_n\hat{\mathbf{s}}}^{c,s;\dagger} \hat{\sigma} f_{\Lambda_n\hat{\mathbf{s}}}^{c,s} = \pm\frac{1}{2} \right\rangle \left| \sum_{0 < |\Lambda - \Lambda_n| < \delta, \hat{\mathbf{s}}} f_{\Lambda\hat{\mathbf{s}}}^{c,s;\dagger} \hat{\sigma} f_{\Lambda\hat{\mathbf{s}}}^{c,s} = 0 \right\rangle, \\ |N_{\Lambda_n}, \pm\frac{1}{2}\rangle_{c,s} &= \left| \sum_{\hat{\mathbf{s}}} f_{\Lambda\hat{\mathbf{s}}}^{c,s;\dagger} \hat{\sigma} f_{\Lambda\hat{\mathbf{s}}}^{c,s} = N_{\Lambda_n}, f_{\Lambda\hat{\mathbf{s}}}^{c,s;\dagger} \sigma_z f_{\Lambda\hat{\mathbf{s}}}^{c,s} = \pm\frac{1}{2} \right\rangle, \\ f_{\Lambda\hat{\mathbf{s}}}^{c,s;\dagger} &= \left[c_{\Lambda,\sigma}^\dagger(\hat{\mathbf{s}}) c_{-\Lambda,-\sigma}(T\hat{\mathbf{s}}) \right], \quad f_{\Lambda\hat{\mathbf{s}}}^{c,s} = \left[c_{\Lambda,\sigma}^\dagger(\hat{\mathbf{s}}) c_{-\Lambda,-\sigma}^\dagger(T\hat{\mathbf{s}}) \right]. \end{aligned} \quad (9)$$

In the above equations the basis states defined via $|f_{\Lambda_n \hat{s}}^{c,s;\dagger} \hat{\sigma} f_{\Lambda_n \hat{s}}^{c,s}\rangle$ refer to pseudo-spins created to take account of charge and spin fluctuations due to longitudinal forward and backward scattering. Similarly the basis states $|N_{\Lambda_n}, \pm \frac{1}{2}\rangle_{c,s}$ formed out by summing the pseudospins over all normal directions \hat{s} in the FS neighbourhood allows exploration of charge/spin fluctuations generated due to tangential scattering. The coefficient $q_l = 1 - q_t$ refer to hybridisation proportions for a pair of electronic states to be involved in longitudinal(l),tangential(t) scattering respectively. While $p_c = 1 - p_s$ refer to charge-spin hybridisation for the fluctuations in the longitudinal channel and $r_c = 1 - r_s$ refer to charge-spin hybridisation for the fluctuations in the tangential channel.

1.2 Gauss-Jordan block diagonalization in the pseudospin Hilbert space

We define projection operators in the basis eq(9) given by $Q_{<\Lambda_n}, Q_{\Lambda_n}, Q_{>\Lambda_n}$, with $0 < \Lambda_n < \Lambda_0$ where Λ_0 is the bare shell width around FS. Here $Q_{<\Lambda_n}, Q_{>\Lambda_n}$ projects pseudospin states in the low (l) and high (h) energy-momentum windows $|\Lambda| < \Lambda_n$ and $|\Lambda| > \Lambda_n$ respectively while Q_{Λ_n} projects pseudospin states on the high energy-momentum pivot (hp) $|\Lambda| = \Lambda_n$. The sum of the projection operators are constrained to yield the completeness relation in the pseudospin basis, $Q_{<\Lambda_n} + Q_{\Lambda_n} + Q_{>\Lambda_n} = 1$. In the pseudo-spin basis the Hubbard Hamiltonian eq(6) can be written as a composition of off-diagonal block matrices in the l, hp subspaces given by $\hat{H}_n^{l, hp} = Q_{<\Lambda_n} \hat{H} Q_{\Lambda_n}$, $\hat{H}_n^{hp, l} = Q_{\Lambda_n} \hat{H} Q_{<\Lambda_n}$ which corresponds to spin flip scattering between those sectors, see orange colored blocks in fig(5(b)). While the red blocks in fig(5(b)) corresponds to a pivot Hamiltonian $H_n^{hp} = Q_{\Lambda_n} \hat{H} Q_{\Lambda_n}$. By performing a Gauss-Jordan pivot folding step while removing connectivities between the l and hp sectors we can relate the Hamiltonians at the end of the nth and n+1th step by a recursive RG equation [14],

$$\hat{H}_{n-1}^l = Q_{<\Lambda_{n-1}} \hat{H}_n^l Q_{<\Lambda_{n-1}} + Q_{<\Lambda_{n-1}} \hat{H}_n^{l, hp} \hat{G}_{hp, n}(E) \hat{H}_n^{hp, l} Q_{<\Lambda_{n-1}}, \quad (10)$$

where $G_{hp,n}(E) = (E - H_n^{hp})^{-1}$.

Pivot Greens function in the pseudospin basis: The pivot Greens function, $\hat{G}_{hp,n}$, has poles in the $E = \pm\omega$ branches for the pseudospin \uparrow / \downarrow states respectively. The quantum energy scale $-\frac{W}{2} < \omega < \frac{W}{2}$ probes electronic states of the non-interacting tight-binding metal. In the pseudospin basis, $\hat{G}_{hp,n}$ can, therefore, be represented as

$$\hat{G}_{hp,n}^{-1}(\omega) = \begin{pmatrix} \hat{G}_{pqr,\hat{s},\uparrow}^{-1}(\omega, \Lambda) - V_{pqr,\hat{s},\uparrow}^{int} & V_{pqr,\hat{s},\uparrow\leftarrow\downarrow}^{int} \\ V_{pqr,\hat{s},\uparrow\rightarrow\downarrow}^{int} & \hat{G}_{pqr,\hat{s},\downarrow}^{-1}(-\omega, \Lambda) - V_{pqr,\hat{s},\downarrow}^{int} \end{pmatrix} \quad (11)$$

where ,

$$\hat{G}_{pqr,\hat{s},\uparrow}^{-1}(\omega) = \omega - q_l(p_c\epsilon_{\Lambda,\hat{s}}^c + p_s\epsilon_{\Lambda,\hat{s}}^s) - q_t(r_c\epsilon_{\Lambda,\text{avg}}^c + r_s\epsilon_{\Lambda,\text{avg}}^s) . \quad (12)$$

Here, the pairing energies for the doublon-holon (c) and spinon (s) excitations constructed around the nodal wave-vector are given by $\epsilon_{\Lambda,\hat{s}}^c = \epsilon_{\Lambda\hat{s}} + \epsilon_{-\Lambda T\hat{s}} - \mu_{eff}$ and $\epsilon_{\Lambda,\hat{s}}^s = \epsilon_{\Lambda\hat{s}} - \epsilon_{-\Lambda T\hat{s}}$ respectively. An average of the energy for doublon-holon/spinon pair over the entire Fermi surface (arising from tangential scattering) is given by $\epsilon_{\Lambda,\text{avg}}^{c,s} = \frac{1}{N_F} \sum_{\hat{s}} \epsilon_{\Lambda,\hat{s}}^{c,s}$ where $N_F = \sum_{\hat{s}} 1$.

2 Renormalization Group equations

2.1 RG equations at half-filling ($\mu_{eff} = 0$)

Renormalization group difference equations for the couplings associated with the forward ($V_{\mathbf{Q}_{\eta\eta'}=(0),\hat{s}}^{c,s}$), backward ($V_{\mathbf{Q}_{\eta\eta'}=(\pi),\hat{s}}^{c,s}$) and tangential ($V_{t\hat{s}}^{c,s}$) scattering can be deduced from the above operator relation eq(10)

$$\begin{aligned} \frac{\Delta V_{\mathbf{Q}_{\eta\eta'}=(0,\pi),\hat{s}}^{c,s}}{\Delta \log(\Lambda/\Lambda_0)} &= \frac{p_{c,s} q_l (V_{\mathbf{Q}_{\eta\eta'},\hat{s}}^{c,s})^2}{e^{i\gamma_{\hat{s}}^{\downarrow,\uparrow}} |G_{pqr,\hat{s},(\downarrow,\uparrow)}^{-1}(\omega, \Lambda)| - q_l \frac{p_c V_{\mathbf{Q}_{\eta\eta'},\hat{s}}^c + p_s V_{\mathbf{Q}_{\eta\eta'},\hat{s}}^s}{4} - N_{\Lambda}(N_{\Lambda} + 1) q_t \frac{r_c V_{t\hat{s}}^c + r_s V_{t\hat{s}}^s}{4}} \\ \frac{\Delta V_{t\hat{s}}^{c,s}}{\Delta \log(\Lambda/\Lambda_0)} &= \frac{(N_{\Lambda}(N_{\Lambda} + 1) - \frac{3}{4}) q_t r_{c,s} (V_{t\hat{s}}^{c,s})^2}{e^{i\gamma_{\hat{s}}^{\downarrow}} |G_{pqr,\hat{s},\downarrow}^{-1}(\omega, \Lambda)| - q_l \frac{p_c V_{\mathbf{Q}_{\eta\eta'},\hat{s}}^c + p_s V_{\mathbf{Q}_{\eta\eta'},\hat{s}}^s}{4} - N_{\Lambda}(N_{\Lambda} + 1) q_t \frac{r_c V_{t\hat{s}}^c + r_s V_{t\hat{s}}^s}{4}} \end{aligned} \quad (13)$$

where $\gamma_{\uparrow,\downarrow}$ is the Topological phase given by $\gamma_{\uparrow,\downarrow} := e^{i\pi(N_{\uparrow,\downarrow}+1)}$ and the topological invariant $N_{\Lambda\hat{s},\mathbf{P}} = \oint dz \mathcal{G}_{\Lambda\hat{s}}^{-1} \partial_z \mathcal{G}_{\Lambda\hat{s}}$. The hybridization proportions ($p_{\omega}, q_{\omega}, r_{\omega}$) are determined from

a maximization of the Greens function $|G_{pqr,\hat{s},\uparrow}(\omega, \Lambda)|$ at every ω . This protocol leads to a dynamical determination of the most singular pole among $G_{pqr,\hat{s},\uparrow}^{-1}(\omega, \Lambda)'s$ at each and every ω . Specialising to the case of half-filling ($\mu_{eff} = 0$), we find that the tangential scattering is marginal as $q_l = (1 - q_t) = 1$ is associated with the fastest growing RG flow. In this way, the electronic states very naturally choose the longitudinal scattering channel for every \hat{s} along the FS. We use the Python language to solve the RG equations numerically in an iterative manner on a two-dimensional grid in momentum-space, obtaining a phase diagram from the fixed point values of various couplings, spectral weights and gaps. Some properties of various phases (e.g., resistivity) are also obtained from these final values.

2.2 Renormalization Group equations with hole doping ($\mu_{eff} = -\frac{U_0}{2}$)

Upon doping away from 1/2-filling, the RG equations are given by

$$\begin{aligned} \frac{\Delta V_{\mathbf{Q}_{\eta\eta'},\hat{s}}^{c,s}}{\Delta \log \Lambda} &= \frac{p_{c,s}(V_{\mathbf{Q}_{\eta\eta'},\hat{s}}^{c,s})^2}{e^{i\gamma_s^{\downarrow,\uparrow}} |G_{p,\hat{s},(\downarrow,\uparrow)}^{-1}(\omega + \mu_{eff}^*, \Lambda)| + p_c(\mu_{eff} - \mu_{eff}^*) - p_c \frac{V_{\mathbf{Q}_{\eta\eta'},\hat{s},n}^c}{4} - p_s \frac{V_{\mathbf{Q}_{\eta\eta'},\hat{s},n}^s}{4}} \\ \frac{\Delta V^t}{\Delta \log \Lambda} &= \frac{(1-q)(N_\Lambda(N_\Lambda + 1) - \frac{3}{4})V^{t2}}{(\omega + \mu_{eff}^*) + \epsilon_{\Lambda,\text{avg}}^c - p_c(\mu_{eff} - \mu_{eff}^*) - N_\Lambda(N_\Lambda + 1)V_{\mathbf{Q}_{\eta\eta'},n}^t}, \end{aligned} \quad (14)$$

where feedback from tangential scattering has been taken account of by updating the kinetic energy of the charge and spin fluctuations via $\epsilon_{\Lambda,\text{avg}}^c$. For $\mu_{eff} > \mu_{eff}^* = -\frac{W}{2}$, we find that tangential scattering is irrelevant, analytically continuing to the $\mu_{eff} \rightarrow 0$ case discussed above. As discussed in the main text, this region displays the collapse of Mottness.

2.3 Quantum critical point

At critical doping $\mu_{eff} = \mu_{eff}^*$, the RG equations for the nodal \hat{s} have the form

$$\begin{aligned}
\frac{\Delta V_{\mathbf{Q}_{\eta\eta'}, \hat{s}_N, n}^c}{\Delta \log \Lambda} &= (1 - \bar{p}) \frac{V_{\mathbf{Q}_{\eta\eta'}, \hat{s}, n}^{c2}}{\left(\omega - \frac{W}{2}\right) - (1 - \bar{p})v_{F\hat{s}_N}\Lambda - \frac{(U_0 - W)}{2} - \frac{V_{\mathbf{Q}_{\eta\eta'}, \hat{s}, n}^c}{4}}, \quad \bar{p} \rightarrow 0, \\
\frac{\Delta V_{\mathbf{Q}_{\eta\eta'}, \hat{s}_N, n}^s}{\Delta \log \Lambda} &= \bar{p} \frac{V_{\mathbf{Q}_{\eta\eta'}, \hat{s}, n}^{s2}}{\left(\omega - \frac{W}{2}\right) - \bar{p}v_{F\hat{s}_N}\Lambda - \frac{(U_0 - W)}{2} - \bar{p}\frac{V_{\mathbf{Q}_{\eta\eta'}, \hat{s}, n}^s}{4}}, \quad \bar{p} \rightarrow 0, \\
\frac{\Delta V_{\mathbf{Q}_{\eta\eta'}, n}^t}{\Delta \log \Lambda} &= \frac{\left(N_\Lambda(N_\Lambda + 1) - \frac{3}{4}\right) V_{\mathbf{Q}_{\eta\eta'}, n}^{t2}}{\left(\omega - \frac{W}{2}\right) - (1 - \bar{p})v_{F\hat{s}_N}\Lambda + \frac{(U_0 - W)}{2} - N_\Lambda(N_\Lambda + 1)V_{\mathbf{Q}_{\eta\eta'}, n}^t}, \quad (15)
\end{aligned}$$

where the nodal excitation velocity scale is $v_{F\hat{s}_N} = W(\epsilon_x - \epsilon_y)$. These equations for the nodal direction show that at the QCP $\mu_{eff} = \mu_{eff}^*$ for $\omega = \omega_{PG}^{c,*} = -\mu_{eff}^*$, tangential and umklapp scattering are RG irrelevant ($\gamma_N^\uparrow = \pi$), charge forward scattering RG relevant and spin forward and backward scattering both marginally irrelevant (as $\bar{p} = 0, \gamma_N^\uparrow = \pi$). On the other hand, at any higher quantum energy scale ($\omega < \omega_{PG}^{c,*} = -\mu_{eff}^*$) and with deviations away from critical doping ($|\mu_{eff} - \mu_{eff}^*| > \delta$), we have enhanced spin-gapping starting from the antinodes (AN0 all the way upto (but not including) the nodes (N). Indeed, the effective Hamiltonian for each of the four gapless nodal metals (corresponding to the four nodal points) at the QCP can be written in terms of $SU(2)$ chiral fermions undergoing forward scattering

$$\begin{aligned}
\hat{H} &= \sum_{\Lambda} v_F \Lambda f_{\Lambda\hat{s}_N}^{c\dagger} \sigma_z f_{\Lambda\hat{s}_N}^c + v_F \Lambda f_{\Lambda-\hat{s}_N}^{c\dagger} \sigma_z f_{\Lambda-\hat{s}_N}^c \\
&+ \frac{V_{\hat{s}_N}}{4} \sum_{\Lambda\Lambda'} (f_{\Lambda-\hat{s}_N}^{c\dagger} \hat{\sigma} f_{\Lambda-\hat{s}_N}^c \cdot f_{\Lambda'-\hat{s}_N}^{c\dagger} \hat{\sigma} f_{\Lambda'-\hat{s}_N}^c + (\hat{s} \rightarrow R_y \hat{s})) \\
&+ \frac{V_{\hat{s}_N}}{4} \sum_{\Lambda\Lambda'} (f_{\Lambda\hat{s}_N}^{c\dagger} \hat{\sigma} f_{\Lambda\hat{s}_N}^c \cdot f_{\Lambda'\hat{s}_N}^{c\dagger} \hat{\sigma} f_{\Lambda'\hat{s}_N}^c + (\hat{s} \rightarrow R_y \hat{s})). \quad (16)
\end{aligned}$$

We will see below that, due to forward scattering via doublon-holon and spinon collective excitations, the electronic quasi-particles attain a finite (i.e., non-diverging) lifetime as the FS is approached $\tau_{qp} \propto \omega^{-1}$. The presence of gapless collective excitations at the FS ensures that the

QCP corresponds to a nodal non-Fermi liquid (also see later discussion on other properties of this metallic state).

2.4 (π, π) Charge density wave, (π, π) Spin density wave and d-wave Superconducting instabilities

We include (π, π) charge density wave and (π, π) spin density wave symmetry breaking fields

$$\begin{aligned}\hat{H} &= \sum_{\hat{s}, \Lambda_n} \frac{1}{4} p_c (|\mu_{eff} - \mu_{eff}^*| + U_{fp, \hat{s}}^c) \Delta_c \left[\left(f_{\Lambda_n \hat{s}}^{c\dagger} \sigma^+ f_{\Lambda_n \hat{s}}^c \right) + h.c. \right] \\ &+ \frac{1}{8} p_s (U_0 + U_{fp, \hat{s}}^s) \Delta_s \left[\left(f_{\Lambda_n \hat{s}}^{s\dagger} \sigma^+ f_{\Lambda_n \hat{s}}^s \right) + h.c. \right],\end{aligned}\quad (17)$$

and perform a RG calculation for the instabilities associated with them. Thus, the RG equations for the CDW and SDW instabilities have the form

$$\begin{aligned}r = 0 \text{ (SDW)} &\rightarrow \frac{\Delta U_{SDW}}{\Delta \log \Lambda} = \frac{(N_\Lambda(N_\Lambda + 1) - \frac{3}{4}) U_{SDW}^2}{G_{r=0, \uparrow, \Lambda}^{-1}(\omega) - N_\Lambda(N_\Lambda + 1) U_{SDW}} \\ r = 1 \text{ (CDW)} &\rightarrow \frac{\Delta U_{CDW}}{\Delta \log \Lambda} = \frac{(N_\Lambda(N_\Lambda + 1) - \frac{3}{4}) U_{CDW}^2}{G_{r=1, \uparrow, \Lambda}^{-1}(\omega) - N_\Lambda(N_\Lambda + 1) U_{CDW}}\end{aligned}\quad (18)$$

where $G_{r, \uparrow, \Lambda}^{-1} = \omega - \sqrt{(E_{kin, \Lambda}^r)^2 + (U_{int}(r))^2}$ for $r = 0, 1$ respectively and the net kinetic energy of the electronic states in the high energy sector is given by,

$$E_{kin, \Lambda}^r = \frac{1}{N} \left[r \sum_{\hat{s}} (\epsilon_{\Lambda \hat{s}} + \epsilon_{-\Lambda T \hat{s}}) + (1 - r) \sum_{\hat{s}} (\epsilon_{\Lambda \hat{s}} - \epsilon_{-\Lambda T \hat{s}}) \right]. \quad (19)$$

The fixed point value of the spin-charge hybridised interaction strength for the symmetry preserved spin($r=0$)/charge($r=1$) fluctuation dominated Mott insulator is

$$U_{int}(r) = (1 - r)(U_0 + U_{fp}^s) \Delta_s + r(|U_0 - U_{0c}| + U_{fp}^c) \Delta_c, \quad (20)$$

where the gap scales in the spin and charge excitation sectors are

$$\begin{aligned}\Delta_{s0} &= N_F^{-1} \sum_{\hat{s}} |\langle f_{\Lambda_n \hat{s}_{\eta'}}^{s\dagger} \sigma^- f_{\Lambda_n \hat{s}_{\eta'}}^s \rangle| = \frac{\Lambda_s^*}{\Lambda_0}, \\ \Delta_{c0} &= N_F^{-1} \sum_{\hat{s}} |\langle f_{\Lambda_n \hat{s}_{\eta'}}^{c\dagger} \sigma^- f_{\Lambda_n \hat{s}_{\eta'}}^c \rangle| = \frac{\Lambda_c^*}{\Lambda_0},\end{aligned}\quad (21)$$

and (U_{fp}^c, U_{fp}^s) are computed from the first level of the RG equations eq(14).

Finally, we add the superconducting fluctuations through a bare uniform U(1) symmetry breaking field

$$\begin{aligned} H_{sc} &= \sum_{\hat{s}_\eta \hat{s}_{\eta'}} V_{sc, \mathbf{Q}_{\eta\eta'}} \tilde{f}_{\Lambda_n \hat{s}_\eta}^{sc\dagger} \boldsymbol{\sigma} \tilde{f}_{\Lambda_n \hat{s}_\eta}^{sc} \cdot \tilde{f}_{\Lambda_n \hat{s}_{\eta'}}^{sc\dagger} \boldsymbol{\sigma} \tilde{f}_{\Lambda_n \hat{s}_{\eta'}}^{sc} \\ H_{sc}^{SB} &= \frac{1}{4} |U_0 - U_{0c}| \sum_{\hat{s}_\eta} \left[f_{\Lambda_n \hat{s}_\eta}^{sc\dagger} \sigma^+ f_{\Lambda_n \hat{s}_\eta}^{sc} + h.c. \right], \end{aligned} \quad (22)$$

defined in terms of the fermion spinor $f_{\Lambda_n \hat{s}_\eta}^{sc\dagger} = [c_{\Lambda_n \hat{s}_\eta}^\dagger c_{\Lambda_n - T \hat{s}_\eta}]$. In order to assess the role of superconducting fluctuations, we first compute the two-electron (Cooper channel) Greens function in the presence of CDW and SDW fluctuations, tangential scattering, a spin pseudogap centered around the antinodes of the FS as well as a gapless nodal non-Fermi liquid metal

$$\begin{aligned} G_{ee, \omega \Lambda_n \hat{s}}^{-1} &= \omega - \tilde{\epsilon}_{\Lambda_n \hat{s}}^{ren}, \quad \tilde{\epsilon}_{\Lambda \hat{s}}^{ren} = \pm \sqrt{\tilde{\epsilon}_{\Lambda \hat{s}}^2 + V_{Q_{\eta\eta'}}^2}, \\ \tilde{\epsilon}_{\Lambda \hat{s}} &= \sqrt{(\epsilon_{\Lambda \hat{s}} + \epsilon_{\Lambda - T \hat{s}})^2 + \frac{1}{4} |U_0 - U_{0c}|^2} + \frac{\Delta_{\Lambda, CDW}^2}{W + \epsilon_{- \Lambda T \hat{s}}} + \frac{\Delta_{\Lambda, SDW}^2}{W - \epsilon_{- \Lambda T \hat{s}} - \frac{\Delta_{\Lambda, CDW}^2}{W + \epsilon_{- \Lambda T \hat{s}}}} \end{aligned} \quad (23)$$

The renormalization group equations then leads to the following RG equations for the superconducting instability at a given \hat{s} as well as at the node (\hat{s}_N)

$$\begin{aligned} \frac{\Delta V_{sc}(\hat{s})}{\Delta \log \Lambda} &= \frac{V_{sc}^2(\hat{s})}{e^{i\gamma_{\hat{s}}} (\epsilon_{\Lambda \hat{s}} + \epsilon_{\Lambda - T \hat{s}}) - V_{sc}(\hat{s})}, \\ \frac{\Delta V_{sc}(\hat{s}_N)}{\Delta \log \Lambda} &= \frac{V_{sc}^2(\hat{s}_N)}{e^{i\gamma_N} (\epsilon_{\Lambda \hat{s}_N} + \epsilon_{\Lambda - T \hat{s}_N}) - V_{sc}(\hat{s}_N)}, \quad \gamma_N = i \ln \text{sgn}(G_{hh, \omega \Lambda_n \hat{s}}^{-1}) = \pi \end{aligned} \quad (24)$$

leading to the fixed point values $\Lambda_{fp}(\hat{s}) = \frac{\Lambda^*(\hat{s})}{\Lambda_0}$, $\Lambda_{fp}(\hat{s}_N) = 0$, and $V_{sc}^* = \epsilon_{\Lambda \hat{s}} + \epsilon_{\Lambda - T \hat{s}}$. From these, we can obtain the expectation value for the d-wave superconducting order parameter

$$\begin{aligned} \langle c_{\Lambda - T \hat{s} \downarrow}^\dagger c_{\Lambda \hat{s} \uparrow}^\dagger \rangle &= e^{i\gamma_{\hat{s}, \hat{s}_N}} \frac{\Lambda^*(\hat{s})}{\Lambda_0} \frac{1}{\sqrt{\left(\frac{\Lambda^*(\hat{s})}{\Lambda_0}\right)^2 + (\tilde{\epsilon}_{\Lambda \hat{s}}^{ren} - \tilde{\epsilon}_{\Lambda \hat{s}_N}^{ren})^2}}, \\ \langle c_{\Lambda - \hat{s} \downarrow}^\dagger c_{\Lambda T \hat{s} \uparrow}^\dagger \rangle &= e^{i\gamma_{T \hat{s}, \hat{s}_N}} \frac{\Lambda^*(\hat{s})}{\Lambda_0} \frac{1}{\sqrt{\left(\frac{\Lambda^*(\hat{s})}{\Lambda_0}\right)^2 + (\tilde{\epsilon}_{\Lambda \hat{s}_N}^{ren} - \tilde{\epsilon}_{\Lambda T \hat{s}}^{ren})^2}}, \\ \langle c_{\Lambda - \hat{s}_N \downarrow}^\dagger c_{\Lambda T \hat{s}_N \uparrow}^\dagger \rangle &= 0, \quad \gamma_{\hat{s}, \hat{s}_N} = i \ln(\text{sgn}(\epsilon_{\Lambda \hat{s}_N}^{ren} - \epsilon_{\Lambda T \hat{s}}^{ren})). \end{aligned} \quad (25)$$

The superconducting fluctuations characterised by $V_{sc,0}/\epsilon_{\Lambda\hat{s}} + \epsilon_{\Lambda-T\hat{s}}$ possess their largest value at the antinodes (AN) and smallest value infinitesimally close to the nodes (N): the gap is, therefore, the largest at AN and vanishes precisely at N. Indeed, the vanishing gap at the nodes arises from the irrelevance of spin backscattering renormalization, which is turn is associated with a hole-occupancy in the high energy sector at the node: $|f_{sc,N}^\dagger(\Lambda, \hat{s})\sigma_z f_{sc,N}(\Lambda, \hat{s}) = -\frac{1}{2}\rangle$. In this way, the effective d-wave structure of the superconducting gap and gapless nodal Dirac fermions associated with Lifshitz criticality is inherited from the state achieved at Mottness collapse ($\omega_{c,PG}^* = 4$). Indeed, critical doping corresponds to the highest (“optimal”) superconducting transition temperature (T_c). It is remarkable that U(1) phase-rotation symmetry-breaking leads to the spread of d-wave superconductivity to an entire region in the $\omega - \mu_{eff}$ phase diagram, i.e., a “dome” that is centered around, but extends well beyond, the neighbourhood of critical doping.

3 Properties of various phases

3.1 Low-energy fixed-point theory

At the stable fixed point reached upon approaching low energies, the Hamiltonian has the form

$$\hat{H}_{fp} = \sum_{\hat{s}} (\hat{H}_{\hat{s} \leq \Lambda^*(\hat{s})} + \hat{H}_{\hat{s} > \Lambda^*(\hat{s})}) , \quad (26)$$

where the effective Hamiltonian for the degrees of freedom within the emergent low-energy window $\hat{s} \leq \Lambda^*(\hat{s})$ is

$$\hat{H}_{\hat{s} \leq \Lambda^*(\hat{s})} = \sum_{\Lambda \leq \Lambda^*(\hat{s}), \hat{s}} \epsilon_{\Lambda\hat{s}}^c f_{\Lambda-\hat{s}_N}^{c\dagger} \sigma_z f_{\Lambda-\hat{s}_N}^c + \epsilon_{\Lambda\hat{s}}^s f_{\Lambda-\hat{s}_N}^{s\dagger} \sigma_z f_{\Lambda-\hat{s}_N}^s + \hat{H}_{<\Lambda^*(\hat{s}), \hat{s}}^{(2)} , \quad (27)$$

with

$$\begin{aligned} \hat{H}_{<\Lambda^*(\hat{s}), \hat{s}}^{(2)} &= \frac{1}{4} \sum_{\Lambda\Lambda' < \Lambda^*(\hat{s}), \hat{s}} V_{\mathbf{Q}_{\eta\eta'}}^{c*}(\omega, \hat{s}) f_{\Lambda\hat{s}_\eta}^{c\dagger} \boldsymbol{\sigma} f_{\Lambda\hat{s}_\eta}^c \cdot f_{\Lambda-T\hat{s}_{\eta'}}^{c\dagger} \boldsymbol{\sigma} f_{\Lambda-T\hat{s}_{\eta'}}^c \\ &+ V_{\mathbf{Q}_{\eta\eta'}}^{s*}(\omega, \hat{s}) f_{\Lambda\hat{s}_\eta}^{s\dagger} \boldsymbol{\sigma} f_{\Lambda\hat{s}_\eta}^s \cdot f_{\Lambda-T\hat{s}_{\eta'}}^{s\dagger} \boldsymbol{\sigma} f_{\Lambda-T\hat{s}_{\eta'}}^s . \end{aligned} \quad (28)$$

The effective Hamiltonian for the degrees of freedom residing outside this low-energy window, $\hat{H}_{\hat{s} > \Lambda^*(\hat{s})}$, can be obtained from the fixed point of the RG procedure in an analogous manner. Henceforth, we will focus our attention on the states lying within the window $\Lambda^*(\hat{s})$. The many body Hilbert space at the stable fixed point with $SU(2)$ spin rotational invariance, $U(1)$ global phase rotational invariance and translational invariance is given by

$$\begin{aligned}
|\Psi(l)\rangle &= \prod_{\hat{s}} \sum_{\mathbf{P}} N_{F,\mathbf{P}}(\hat{s}) \Psi_{\mathbf{P}, \leq \Lambda^*(\hat{s}), \hat{s}}^\dagger(l_{\mathbf{P}}) \Psi_{> \Lambda^*(\hat{s})}^\dagger |0\rangle \\
\Psi_{\mathbf{P}=(0,\pi), \leq \Lambda^*(\hat{s}), \hat{s}}^\dagger &= \mathcal{N}(\hat{s}) \sum_n e^{inl_{0,\pi}} (A_{1, \leq \Lambda^*(\hat{s})}^+)^{l_{0,\pi}} (A_{2, \leq \Lambda^*(\pm\hat{s})}^+)^{N_{\Lambda^*(\hat{s})} - l_{0,\pi}} \\
\Psi_{> \Lambda^*(\hat{s})}^\dagger &= \prod_{\Lambda_j > \Lambda^*(\hat{s}), j=1}^{N_e, F - N_{\Lambda^*(\hat{s})}} (p_c f_{\Lambda_j \hat{s}}^{c\dagger} \sigma^+ f_{\Lambda_j \hat{s}}^c + p_s f_{\Lambda_j \hat{s}}^{s\dagger} \sigma^+ f_{\Lambda_j \hat{s}}^s)
\end{aligned} \tag{29}$$

where,

$$\begin{aligned}
\mathbf{A}_{\leq \Lambda^*(\hat{s})} &= \mathbf{A}_{1, \leq \Lambda^*(\hat{s})} + \mathbf{A}_{2, \leq \Lambda^*(\hat{s})}, \\
\mathbf{A}_{1, \leq \Lambda^*(\hat{s})} &= \sum_{|\Lambda| \leq \frac{1}{2} \Lambda^*(\hat{s})} p_c f_{\Lambda \hat{s}}^{c\dagger} \frac{\boldsymbol{\sigma}}{2} f_{\Lambda \hat{s}}^c + p_s f_{\Lambda \hat{s}}^{s\dagger} \frac{\boldsymbol{\sigma}}{2} f_{\Lambda \hat{s}}^s, \\
\mathbf{A}_{2, \leq \Lambda^*(\hat{s})} &= \sum_{\Lambda^*(\hat{s}) > |\Lambda| > \frac{1}{2} \Lambda^*(\hat{s})} [p_c f_{\Lambda \hat{s}}^{c\dagger} \frac{\boldsymbol{\sigma}}{2} f_{\Lambda \hat{s}}^{c\dagger} + p_s f_{\Lambda \hat{s}}^{s\dagger} \frac{\boldsymbol{\sigma}}{2} f_{\Lambda \hat{s}}^s],
\end{aligned}$$

and $f_{\Lambda \hat{s}} = [c_{\Lambda \hat{s} \sigma} c_{-\Lambda T \hat{s} - \sigma}^\dagger]$ is the electron spinor shown earlier. For $\nu = N_e/(2N) = 1/2$ (half-filling, N_e is the total number of electrons in the system and N is the total number of sites), the emergent particle-hole symmetry at this filling arises in the basis states from $A_{\leq \Lambda^*(\hat{s})}^z + A_{\leq \Lambda^*(-\hat{s})}^z = 0$. This many-body basis corresponds to eigenstates of total number operator and total momentum.

3.2 Benchmarking against existing numerical results

In order to benchmark the results obtained from the effective low-energy Hamiltonian and wavefunctions given above against those found from existing numerical methods applied to the 2D

Hubbard model on the square lattice [5], we present results for the ground state energy per particle E_g and the fraction of bound pairs (Bp) in the gapped Mott liquid ground state. The analytic form for E_g and Bp are computed from the spin and charge backscattering parts $H_{<\Lambda^*(\hat{s}),\hat{s}}^{(2)}$ of the effective Hamiltonian given above, and are found to be

$$E_g = -\frac{4\pi^2}{\sum_{\hat{s}} n_{E_F,\hat{s}}} \sum_{\hat{s}} V_{\mathbf{Q}=\pi,\Lambda^*(\hat{s})}^* \left(\frac{\Lambda^*(\hat{s})}{\Lambda_0}\right)^2, \quad (30)$$

$$Bp = \frac{\sum_{\hat{s}} \Lambda^*(\hat{s})}{\Lambda_0 \sum_{\hat{s}} n_{E_F,\hat{s}}} \quad (31)$$

where $n_{E_F,\hat{s}} = 1$ are the number of electronic states at every point on the Fermi surface with normal \hat{s} , $\Lambda^*(\hat{s})/\Lambda_0$ is the corresponding renormalised low-energy window width for bound-states of the Mott liquid fixed point theory. The fraction of unbound pairs (equivalent to the fraction of double occupied states) is given by $Ubp = 1 - Bp$. The plots for E_g and (Bp, Ubp) versus the probe energy scale ω are shown in Figs.(6) and (7) respectively. A comparison of the saturation value of the ground state energy for the largest k -space grid used in our simulations ($2^{15} \times 2^{15}$), $E_{gs} = -0.505t$ (shown in Fig.(6)), is considerably close to the range $-0.51t < E_{gs} < -0.53t$ obtained in the thermodynamic limit from nine state-of-the-art numerical methods applied to the half-filled 2D Hubbard model at $U = 8t$ [5]. Similarly, the average saturation value for the fraction of unbound pairs in the Mott liquid obtained from a finite-size scaling analysis (inset of Fig.(7)), $Ubp \sim 0.051$, is also found to be considerably close to the range $0.0535 < Ubp < 0.0545$ obtained in Ref.[5].

3.3 Lifetimes and the f-sum rule

Quasiparticles, doublon-holon and two-spinon collective excitations are found to reside within the low-energy window in the metallic regions. In the insulating region, the low-energy window is constituted of doublon-holon and/or two spinon bound pairs. The doublon-holon collective excitations are highly entangled objects formed out of pairs of electrons around the N points.

These are exact eigenstates of the two particle forward-scattering interactions. On the other hand, quasi-particle(hole) states are eigenstates of the Hartree and the kinetic energy parts of the final renormalized Hamiltonian H_{fp} . Similarly, in the insulating regions, the doublon-holon bound pairs are also highly entangled objects, being exact eigenstates of the Umklapp scattering interaction. The lifetime for the quasiparticles (τ_{qp}), bound-pair/gapless collective excitations (τ_{coll}) and fractionally-charged topological excitations ($\tau_{top-exc}$) are given by the following relations [13]

$$\begin{aligned}
\tau_{qp}(\bar{\omega}, \hat{s}) &= \text{Im} \sum_{\Lambda > \Lambda^*(\hat{s})} \int_{-\infty}^{\infty} dt e^{i\bar{\omega}t} \langle \Psi_{exc, \Lambda}^l | \hat{n}_{\Lambda \hat{s} \sigma}^{fp}(t) | \Psi_{exc, \Lambda}^l \rangle \\
\tau_{coll}(\bar{\omega}, \hat{s}) &= \frac{m}{\nu e^2} \lim_{\Phi \rightarrow 0} \frac{d^2 \langle \Psi^l(\Phi) | \hat{H}_{fp} | \Psi^l(\Phi) \rangle}{d\Phi^2} \\
\tau_{top-exc}(\bar{\omega}, \hat{s}) &= \frac{m}{\nu e^2} \lim_{\Phi \rightarrow \Phi_0} \frac{d^2 \langle \Psi^l(\Phi) | \hat{H}_{fp} | \Psi^l(\Phi) \rangle}{d\Phi^2}, \tag{32}
\end{aligned}$$

where $\hat{n}_{\Lambda \hat{s} \sigma}^{fp}(t) = e^{iH_{fp}t} \hat{n}_{\Lambda \hat{s} \sigma} e^{-iH_{fp}t}$ is the time-evolved fermion-number operator, and the state $|\Psi_{exc, \Lambda}^l\rangle = \sum_{\bar{\Lambda} < \Lambda^*(\hat{s})} c_{\bar{\Lambda} \hat{s} \sigma}^\dagger c_{\Lambda \hat{s} \sigma} |\Psi(l), N_e\rangle$. Total spectral weight is conserved via the f-sum rule by integrating the lifetimes of the quasiparticles and collective excitations over the full frequency range. In this way, we are able to take account of the conversion of quasi-particle poles at and around the Fermi surface (within the low-energy window Λ^* for every \hat{s}) into the poles of the two-particle pseudospin electron pairs [27]

$$f = \int d\bar{\omega} (\tau_{qp}(\bar{\omega}, \hat{s}) + \tau_{coll}(\bar{\omega}, \hat{s})) = \nu = \frac{N_e}{N} = 1 \tag{33}$$

3.4 Formation of Bound state

The RG relevant forward scattering coupling leads to the formation of a pole of two-particle (doublon-holon) gapless collective excitations at (and in the neighbourhood of) the Fermi surface. In Fig.(S8(a) (left panel)), this is observed through a crossing of the total phase $\Phi_{FS}(=$

$\sum_{\Lambda_0}^0 G_{\hat{s},\downarrow}^{-1}(\omega, \Lambda)$) of the two-particle forward scattering Greens function in the doublon-holon basis (red line) crossing the energy scale for quantum fluctuations associated with the inverse bare interaction strength ΔU_0^{-1} . As will be discussed below, this leads to a renormalisation of the one-particle Greens function at a given point on the Fermi surface, turning them *marginal* in nature. Similarly, in Fig.(S8(a) (right panel)), we observe the formation of a two-particle doublon-holon bound state at a given point on the Fermi surface (blue line for total phase $\Phi_{BS}(= \sum_{\Lambda_0}^0 G_{\hat{s},\uparrow}^{-1}(\omega, \Lambda))$ crossing ΔU_0^{-1}) arising from a RG relevant backscattering coupling. This is concomitant with a zero of the single-particle Greens function. Indeed, this is analogous to Cooper's demonstration of the formation of bound pairs of electrons leading to an instability of the Fermi surface as being responsible for the onset of superconductivity [47].

3.5 Quasiparticle Lifetime, residue and resistivity of the non-Fermi liquid phase

Our RG delivers microscopic evidence for several key aspects of the phenomenology of the marginal Fermi liquid (see [28]). This can be seen as follows. The single particle green function in the presence of forward scattering gets renormalized due to doublon-holon or two-spinon excitations being present at the vicinity of E_F has the following form,

$$G_{\Lambda\sigma}(\hat{s}) = \frac{1}{\omega - \epsilon_{\Lambda}(\hat{s}) - iV_{\Lambda*\hat{s}}} , \quad (34)$$

where $V_{\Lambda*\hat{s}}(\omega) = p_c \epsilon_{c,\Lambda*}(\hat{s}) + p_s \epsilon_{s,\Lambda*}(\hat{s}) - \omega$ with $\Lambda^*(\hat{s})/\Lambda_0$ being a fraction of the spectral weight along a given normal direction \hat{s} of the doublon-holon/two-spinon collective excitations (Fig.(S8)). The complementary fraction $(1 - \frac{\Lambda^*(\hat{s})}{\Lambda})$ constitute electronic quasiparticles whose spectral function get broadened due to these collective excitations, rendering them with a non-diverging lifetime at low-energies (using eq.(32))

$$\tau_{qp} = \frac{1}{V_{\Lambda*\hat{s}}} \propto \frac{1}{\frac{W}{2} - \omega} . \quad (35)$$

This is shown in Fig.(S9)(c), and displays an enhanced dissipation of quasiparticle excitations in the marginal Fermi liquid (see[28]) due to collisions with doublon-holon collective excitations discussed above.

Another striking feature of this marginal Fermi liquid is the vanishing of the quasiparticle residue $Z_{\Lambda\hat{s}\sigma}$ at low energies. This can be computed from the $Re(\Sigma)$ which can be in turn computed from the $Im(\Sigma)$ via the Kramer Kronig relations,

$$\begin{aligned}
Re(\Sigma) &= \int_{-\infty}^{\infty} d\omega' \frac{V_{\Lambda^*\hat{s}}(\omega')}{\omega' - \omega} = V_{\Lambda^*\hat{s}}(\omega) \ln(W/(W - 2\omega)) \\
Z_{\Lambda\hat{s}}^{-1} &= \left(1 - \frac{dRe(\Sigma)}{d(\frac{W}{2} - \omega)} \right) \Big|_{\frac{W}{2} - \omega \rightarrow \varepsilon_{\Lambda^*}(\hat{s})} = 1 + \frac{dRe(\Sigma)}{d\omega} \Big|_{\frac{W}{2} - \omega \rightarrow p_c \varepsilon_{c,\Lambda^*}(\hat{s}) + p_s \varepsilon_{s,\Lambda^*}(\hat{s})} \\
&= \log(W/\varepsilon_{\Lambda^*}(\hat{s})) , \quad \varepsilon_{\Lambda^*}(\hat{s}) = p_c \varepsilon_{c,\Lambda^*}(\hat{s}) + p_s \varepsilon_{s,\Lambda^*}(\hat{s})
\end{aligned} \tag{36}$$

Indeed, a divergent enhancement in the effective mass $Z^{-1} \sim (m^*/m)$ is shown in Fig.(S10). Further, this leads to a linear variation of the resistivity ρ with the energy scale for quantum fluctuations $4 - \omega$ shown below in Fig.(S11) (also shown to some extent in Figs.1(c), 2(b), 4(c,d) of the main text). Further insights and results will be provided in a later section from the viewpoint of the renormalised single particle propagator and self-energy.

3.6 Pseudogap progression, Fermi arc and topological excitations of the Mott liquid

In Fig. (S9)(a) and (b), we observe the pseudogapping of the spectral function at (and near) the antinodes. The gradual growth in the extent of the pseudogap for charge excitations (shown as a width of the k -space window around the Fermi surface $\bar{\Lambda}$) is shown in Fig.(S7), finally saturating at a finite value when the entire Fermi surface is gapped (the Mott liquid). The inset of Fig.(S7) shows the finite-size scaling of the saturated value of the window width, $\bar{\Lambda}_s$ (proportional to the many-body gap of the Mott liquid), with $\log_2 \sqrt{N}$ (where N is the system size): the plot appears to saturate at a finite value.

As the pseudogap for charge and spin excitations is bookended by Fermi surface topology-changing Lifshitz transitions at the antinode (initial) and node (final) respectively, we show below in Fig.(S12) the finite-size scaling of the energy scales for the entry (ω_{c1} (cyan), ω_{s1} (red)) and exit (ω_{c2} (violet) and ω_{s2} (blue)) of the charge (c) and spin (s) pseudogaps respectively with $\log_2 \sqrt{N}$ (where N is the system size). We can clearly see that the extent of the charge and spin pseudogaps, i.e., the differences $\omega_{c2} - \omega_{c1}$ and $\omega_{s2} - \omega_{s1}$ saturate with increasing system size. Further, the size of the spin pseudogap is dominant over that of the charge pseudogap in the thermodynamic limit. This impacts the growth of the d-wave superconducting order upon doping. Further, the influence of the pseudogap on the resistivity has already been shown in the main manuscript, as well as in Fig.(S11).

In Fig.(S13), we show the gradual decrease of the length of the gapless Fermi surface (i.e., the *Fermi arc*) with gradual progression of the pseudogap phase towards the Mott liquid state (zero Fermi arc-length) [24]. Finally, in Fig.(S14(a)) (left panel), we show the spectral weight for fractionally charged excitations of a topologically ordered state of matter (residing within the charge gapped regions of the pseudogap phase) arising from the application of a charge-twist operator (see main manuscript for details). In Fig(S14(a)) (right panel), we show the lifetime for the same topological excitations within the Mott liquid (i.e., fully gapped Fermi surface). (b) RG phase diagrams at (left panel), and away from (right panel), 1/2-filling. Red dots in both phase diagrams indicate spin and charge gapped phases of topologically ordered Mott liquid state of matter possessing the fractional excitations shown in (a). An analogous result is found for the spectral weight of fractional excitations arising from a spin twist operator applied to the Mott liquid. This is a typical signature of a short-range entangled resonating valence bond (RVB) spin liquid state [12].

3.7 Statistical quantum criticality and fermion signs

In the main text, we observed that the collapse of Mottness, i.e., the vanishing of the energy scale related to the entry into the pseudogap for charge (doublon-holon) excitations, led to a quantum critical point (QCP). This QCP involved the transition from a gapped Mott liquid state with topological order (and an exchange statistics angle of $\theta = \pi/2$ for its fractionally charged excitations) to a correlated Fermi liquid with electronic quasiparticle excitations (obeying the Pauli exclusion principle) at a connected Fermi surface. The QCP was also shown to possess a critical Fermi surface at the four nodal points with a non-Fermi liquid metallic state (composed of gapless collective excitations that couple the spin and charge sectors) arising from RG relevant forward scattering on the four isolated nodal Fermi-points. Such a QCP (involving a drastic change in the exchange statistics of the excitations above the ground state) has been dubbed as *statistical quantum criticality* (or *fermionic quantum criticality*) by Zaanen and Overbosch [34]. Here, we clarify how the well-known problem associated with fermion signs in Euclidean path-integral formulations of fermionic quantum many-body systems allows for such a QCP. First, note that the Fermi liquid itself corresponds to a sign-full path integral. However, as shown in Refs.[48, 49], this path integral can be evaluated in totality without the worrisome *negative probabilities* arising from the exchange of fermions. Further, the gapped Mott liquid state clearly does not suffer from any fermion sign issues. Finally, it was shown in Refs.[50, 51] that the fermion sign problem is mitigated in systems involving non-relativistic interacting fermionic excitations on isolated patches of the Fermi surface. This shows that the nodal non-Fermi liquid metal emergent at the QCP (and which is adiabatically connected to the non-Fermi liquid living at a connected Fermi surface at high energies) is free from fermion sign-related negative probabilities. This offers hope that quantum Monte Carlo simulations of the low-energy effective Hamiltonian reached from our $T = 0$ RG procedure can be used to compute thermodynamic quantities at finite- T without encountering the sign problem.

4 Renormalized single particle green function

We attain the following longitudinal,tangential scattering interactions at the nth step of the RG flow ($\Lambda_n = \Lambda_0 b^n$) and ω ,

$$\begin{aligned}
H_{int}^{low} &= \sum_{\eta\eta', \hat{s}, \Lambda\Lambda' \leq \Lambda_n} V_{\mathbf{Q}_{\eta\eta'}, \hat{s}, n}^c(\omega) f_{\Lambda\hat{s}\eta}^{c\dagger} \vec{\sigma} f_{\Lambda\hat{s}\eta}^c \cdot f_{\Lambda'\hat{s}\eta'}^{c\dagger} \vec{\sigma} f_{\Lambda'\hat{s}\eta'}^c + \sum_{\hat{s}\hat{s}' \Lambda\Lambda' \leq \Lambda_n} V_n^{ct}(\omega) f_{\Lambda\hat{s}}^{c\dagger} \vec{\sigma} f_{\Lambda\hat{s}}^c \cdot f_{\Lambda'\hat{s}'}^{c\dagger} \vec{\sigma} f_{\Lambda'\hat{s}'}^c \\
&+ \sum_{\eta\eta', \hat{s}, \Lambda\Lambda' \leq \Lambda_n} V_{\mathbf{Q}_{\eta\eta'}, \hat{s}, n}^s(\omega) f_{\Lambda\hat{s}\eta}^{s\dagger} \vec{\sigma} f_{\Lambda\hat{s}\eta}^s \cdot f_{\Lambda'\hat{s}\eta'}^{s\dagger} \vec{\sigma} f_{\Lambda'\hat{s}\eta'}^s + \sum_{\hat{s}\hat{s}' \Lambda\Lambda' \leq \Lambda_n} V_n^{st}(\omega) f_{\Lambda\hat{s}}^{s\dagger} \vec{\sigma} f_{\Lambda\hat{s}}^s \cdot f_{\Lambda'\hat{s}'}^{s\dagger} \vec{\sigma} f_{\Lambda'\hat{s}'}^s, \\
H_{int}^{high} &= \sum_{\eta\eta', \hat{s}, \Lambda \geq \Lambda_n} V_{\mathbf{Q}_{\eta\eta'}, \hat{s}, n}^c(\omega) f_{\Lambda\hat{s}\eta}^{c\dagger} \vec{\sigma} f_{\Lambda\hat{s}\eta}^c \cdot f_{\Lambda\hat{s}\eta'}^{c\dagger} \vec{\sigma} f_{\Lambda\hat{s}\eta'}^c + \sum_{\hat{s}\hat{s}' \Lambda \geq \Lambda_n} V_n^{ct}(\omega) f_{\Lambda\hat{s}}^{c\dagger} \vec{\sigma} f_{\Lambda\hat{s}}^c \cdot f_{\Lambda\hat{s}'}^{c\dagger} \vec{\sigma} f_{\Lambda\hat{s}'}^c \\
&+ \sum_{\eta\eta', \hat{s}, \Lambda \geq \Lambda_n} V_{\mathbf{Q}_{\eta\eta'}, \hat{s}, n}^s(\omega) f_{\Lambda\hat{s}\eta}^{s\dagger} \vec{\sigma} f_{\Lambda\hat{s}\eta}^s \cdot f_{\Lambda\hat{s}\eta'}^{s\dagger} \vec{\sigma} f_{\Lambda\hat{s}\eta'}^s + \sum_{\hat{s}\hat{s}' \Lambda \geq \Lambda_n} V_n^{st}(\omega) f_{\Lambda\hat{s}}^{s\dagger} \vec{\sigma} f_{\Lambda\hat{s}}^s \cdot f_{\Lambda\hat{s}'}^{s\dagger} \vec{\sigma} f_{\Lambda\hat{s}'}^s \quad (37)
\end{aligned}$$

The kinetic energy cost for the spin and charge pseudospins is given by,

$$\begin{aligned}
H^{kin} &= \sum_{\Lambda\hat{s}} \epsilon_{\Lambda\hat{s}}^c f_{\Lambda\hat{s}}^{c\dagger} \sigma_z f_{\Lambda\hat{s}}^c + \epsilon_{\Lambda\hat{s}}^s f_{\Lambda\hat{s}}^{s\dagger} \sigma_z f_{\Lambda\hat{s}}^s, \\
\epsilon_{\Lambda\hat{s}}^c &= \epsilon_{\Lambda\hat{s}} + \epsilon_{-\Lambda T\hat{s}} + \frac{U_0}{2}, \quad \epsilon_{\Lambda\hat{s}}^s = \epsilon_{\Lambda\hat{s}} - \epsilon_{-\Lambda T\hat{s}} \quad (38)
\end{aligned}$$

The recursive renormalization group equations for the longitudinal and tangential scattering events are given by,

$$\begin{aligned}
V_{\mathbf{Q}_{\eta\eta'}=(0,\pi), \hat{s}, n+1}^{c,s} &= V_{\mathbf{Q}_{\eta\eta'}=(0,\pi), \hat{s}, n}^{c,s} + \frac{p_{c,s} (V_{\mathbf{Q}_{\eta\eta'}, \hat{s}, n}^{c,s})^2}{G_{p, \hat{s}, (\uparrow, \downarrow)}^{-1}(\omega, \Lambda_n) - p_c \frac{V_{\mathbf{Q}_{\eta\eta'}, \hat{s}, n}^c}{4} - p_s \frac{V_{\mathbf{Q}_{\eta\eta'}, \hat{s}, n}^s}{4}} \\
V_{n+1}^t &= V_n^t + \frac{(N_\Lambda(N_\Lambda + 1) - \frac{3}{4}) (V_n^t)^2}{G_{t, \downarrow}^{-1}(\omega, \Lambda_n) - N_\Lambda(N_\Lambda + 1) V_n^t}, \quad V_n^t = V_n^{ct} \quad (39)
\end{aligned}$$

The green function written down in the pseudospin basis for the longitudinal and tangential scattering basis,

$$\begin{aligned}
\hat{G}_{p, \hat{s}, (\uparrow, \downarrow)}^{-1}(\omega, \Lambda_n) &= e^{i\gamma_{\hat{s}}^{\uparrow, \downarrow}} |\omega - \sqrt{(p_c \epsilon_{\Lambda_n, \hat{s}}^c + p_s \epsilon_{\Lambda_n, \hat{s}}^s)^2 + V_{tn}^2}|, \\
\gamma_{\hat{s}}^{\uparrow} + \gamma_{\hat{s}}^{\downarrow} &= \pi, \quad \gamma_{\hat{s}}^{\uparrow} = \ln(\text{sgn}(\hat{G}_{p, \hat{s}, (\uparrow)}^{-1}(\omega, \Lambda_n))) \\
G_{t, \downarrow}^{-1}(\omega, \Lambda_n) &= e^{i\gamma_{t, \downarrow}} |\omega + \frac{U_0}{2} - W + \frac{1}{N_F} \sum_{\hat{s}} \epsilon_{\Lambda_n, \hat{s}}^c|, \\
\gamma_{t, \downarrow} &= \ln(\text{sgn}(G_{t, \downarrow}^{-1}(\omega, \Lambda_n))) \quad (40)
\end{aligned}$$

where $N_F(\hat{s}) = \sum_{\hat{s}} 1$ is the number of normal directions on the Fermi surface, $p_c = 1 - p_s = p$. The hybridization proportions p_ω is determined from the maximization of the green function $|G_{p,\hat{s},\uparrow}(\omega, \Lambda)|$ overall \hat{s}' at every ω which is the quantum energy scale varying from $0 < \frac{W}{2} - \omega < W$, with $W=8t$ being the bandwidth . This protocol leads to the most singular pole among $G_{p,\hat{s},\uparrow}^{-1}(\omega, \Lambda)'s$ being dynamically determined at each and every quantum energy scale.

4.1 Representing four Fermi interaction in terms of pseudospins coupled to fermion

The four fermi interaction in the pseudospin basis can be rewritten in terms of the three fermion composite operator and a fermion,

$$\begin{aligned}
H_{int}^{low} = & \sum_{\Lambda, \eta\eta', \hat{s}, \sigma} V_{\mathbf{Q}_{\eta\eta'=(0,\pi), \hat{s}, n}}^c(\omega) \left(M_{\Lambda, \Lambda', \hat{s}_\eta, \hat{s}_{\eta'}, \sigma}^{c\dagger} c_{\Lambda \hat{s}_{\eta'} \sigma} + h.c. \right) \\
& + \sum_{\Lambda, \eta\eta', \hat{s}, \sigma} V_{\mathbf{Q}_{\eta\eta'=(0,\pi), \hat{s}, n}}^s(\omega) \left(M_{\Lambda, \Lambda', \hat{s}_\eta, \hat{s}_{\eta'}, \sigma}^{s\dagger} c_{\Lambda \hat{s}_{\eta'} \sigma} + h.c. \right) \\
& + \sum_{\Lambda, \hat{s}\hat{s}'\sigma} V_n^t(\omega) \left(M_{\Lambda, \Lambda', \hat{s}, \hat{s}', \sigma}^{c\dagger} c_{\Lambda \hat{s}' \sigma} + h.c. \right) \\
& + \sum_{\eta\eta', \hat{s}, \Lambda\Lambda' \leq \Lambda_n} V_{\mathbf{Q}_{\eta\eta', \hat{s}, n}}^c(\omega) f_{\Lambda \hat{s}_\eta}^{c\dagger} \vec{\sigma} f_{\Lambda \hat{s}_\eta}^c \cdot f_{\Lambda' \hat{s}_{\eta'}}^{c\dagger} \sigma_z f_{\Lambda' \hat{s}_{\eta'}}^c + \sum_{\hat{s}\hat{s}' \Lambda\Lambda' \leq \Lambda_n} V_n^{ct}(\omega) f_{\Lambda \hat{s}}^{c\dagger} \vec{\sigma} f_{\Lambda \hat{s}}^c \cdot f_{\Lambda' \hat{s}'}^{c\dagger} \sigma_z f_{\Lambda' \hat{s}'}^c \\
& + \sum_{\eta\eta', \hat{s}, \Lambda\Lambda' \leq \Lambda_n} V_{\mathbf{Q}_{\eta\eta', \hat{s}, n}}^s(\omega) f_{\Lambda \hat{s}_\eta}^{s\dagger} \sigma_z f_{\Lambda \hat{s}_\eta}^s \cdot f_{\Lambda' \hat{s}_{\eta'}}^{s\dagger} \sigma_z f_{\Lambda' \hat{s}_{\eta'}}^s
\end{aligned} \tag{41}$$

where $M_{\Lambda' \Lambda \hat{s} \sigma}^{c,s}$ is given by,

$$M_{\Lambda, \Lambda', \hat{s}_\eta, \hat{s}_{\eta'}, \sigma}^{c\dagger} = f_{\Lambda' \hat{s}_{\eta'}}^{c\dagger} \sigma_z f_{\Lambda \hat{s}_\eta}^c c_{-\Lambda T \hat{s}_{\eta'} - \sigma} \ , \ M_{\Lambda, \Lambda', \hat{s}_\eta, \hat{s}_{\eta'}, \sigma}^{s\dagger} = f_{\Lambda' \hat{s}_{\eta'}}^{s\dagger} \sigma_z f_{\Lambda \hat{s}_\eta}^s c_{-\Lambda T \hat{s}_{\eta'} - \sigma}^{\dagger} \ . \tag{42}$$

4.2 Coupling Fermi surface pseudospins to Fermionic states in offset curves

We will now reduce down to a effective Hamiltonian involving the coupling between pseudospins at the Fermi energy with the offset curves at Λ for every normal direction \hat{s} , this is

motivated on the perspective of arriving at low energy single electron green function due to scattering fermions from the bare Fermi surface,

$$\begin{aligned}
H_{int}^{low} \rightarrow H_{F,int}^{low} &= \sum_{\Lambda, \eta \eta', \hat{s}, \sigma} V_{\mathbf{Q}_{\eta \eta'}=(0, \pi), \hat{s}, n}^c(\omega) \left(M_{F\Lambda, \hat{s}\eta, \hat{s}\eta', \sigma}^{c\dagger} c_{\Lambda \hat{s}\eta' \sigma} + h.c. \right) \\
&+ \sum_{\Lambda, \eta \eta', \hat{s}, \sigma} V_{\mathbf{Q}_{\eta \eta'}=(0, \pi), \hat{s}, n}^s(\omega) \left(M_{F\Lambda, \hat{s}\eta, \hat{s}\eta', \sigma}^{s\dagger} c_{\Lambda \hat{s}\eta' \sigma} + h.c. \right) \\
&+ \sum_{\Lambda, \hat{s} \hat{s}' \sigma} V_n^t(\omega) \left(M_{F\Lambda, \hat{s}, \hat{s}', \sigma}^{c\dagger} c_{\Lambda \hat{s}' \sigma} + h.c. \right), \tag{43}
\end{aligned}$$

where $M_{F\Lambda, \hat{s}\eta, \hat{s}\eta', \sigma}^{c, s; \dagger} = f_{F\hat{s}\eta}^{c, s; \dagger} \sigma^+ f_{F\hat{s}\eta}^{c, s} (c_{-\Lambda T \hat{s}\eta' - \sigma} \text{ or } c_{-\Lambda T \hat{s}\eta' - \sigma}^\dagger)$

4.3 Computing the imaginary piece of self energy matrix from the pseudospin fermion Hamiltonian

From the renormalized two particle vertex at the final fixed point we determine the single particle self energy by considering the integrating out of virtual states described as a pseudospin coupled to a fermion. This leads us contracting two two particle vertices and gathering a six fermion term $2 \times (2\text{pseudospin} + 1\text{fermion})$ which can be written as a product of three single particle green function and corresponds to the mathematical form of $\Sigma^{(II)}$ [53]. This integrating out leads to a two fermion scattering processes 1) forward scattering processes that causes life-time broadening for the single fermion quasiparticles and residue Z decay , 2) backscattering processes that causes pole to zero conversion for single particle states. Below the figure fig(15) represents the scattering process. The connectivity term between single electronic states in the neighbourhood of one direction along the Fermi surface \hat{s} and scattering to a opposite direction $\hat{s} \rightarrow -\hat{s}$ can be arrived at by pivot folding the fermionic states coupled to the Fermi surface pseudospins eq(43) leading to a imaginary self energy matrix,

$$\hat{\Sigma}_{\Lambda, \hat{s}, n}^{Im}(\omega) = f_{\Lambda, \hat{s}, \sigma}^\dagger \hat{K}_{\Lambda, \hat{s}, \sigma} f_{\Lambda, \hat{s}, \sigma}, \quad \hat{K}_{\Lambda, \hat{s}, \sigma} = \begin{pmatrix} \Sigma_{\Lambda, \hat{s}, n}^{Im++}(\omega) & \Sigma_{\Lambda, \hat{s}, n}^{Im+-}(\omega) \\ \Sigma_{\Lambda, \hat{s}, n}^{Im-+}(\omega) & \Sigma_{\Lambda, \hat{s}, n}^{Im--}(\omega) \end{pmatrix}, \quad f_{\Lambda, \hat{s}, \sigma}^\dagger = \left(c_{\Lambda \hat{s}+1 \sigma}^\dagger c_{\Lambda \hat{s}-1 \sigma} \right) \tag{44}$$

where $\eta = \pm 1$ represents the directions \hat{s} , $-\hat{s}$ respectively. The components of the self energy matrix is computed,

$$\begin{aligned} \Sigma_{\Lambda, \hat{s}, n}^{Im\eta\eta'}(\omega) &= \int d\bar{\omega} d\Lambda' \langle 0_{\Lambda \hat{s} \eta \sigma} 1_{\Lambda' \hat{s} \eta' \sigma} | V_{\mathbf{Q}_{\eta\eta'}, \hat{s}, n}^c(\omega) c_{\Lambda \hat{s} \eta \sigma}^\dagger M_{F\Lambda, \hat{s} \eta, \hat{s} \eta', \sigma}^c(\bar{\omega}) G_{F, \Lambda, \Lambda', \hat{s} \eta, \hat{s} \eta'}^c \\ &\quad V_{\mathbf{Q}_{\eta\eta'}, \hat{s}, n}^c(\omega) M_{F\Lambda', \hat{s} \eta, \hat{s} \eta', \sigma}^{c\dagger}(\bar{\omega}) c_{\Lambda' \hat{s} \eta' \sigma} | 0_{\Lambda \hat{s} \eta \sigma} 1_{\Lambda' \hat{s} \eta' \sigma} \rangle \\ &+ \int d\bar{\omega} d\Lambda' \langle 0_{\Lambda \hat{s} \eta \sigma} 1_{\Lambda' \hat{s} \eta' \sigma} | V_{\mathbf{Q}_{\eta\eta'}, \hat{s}, n}^s(\omega) c_{\Lambda \hat{s} \eta \sigma}^\dagger M_{F\Lambda, \hat{s} \eta, \hat{s} \eta', \sigma}^s(\bar{\omega}) G_{F, \Lambda, \Lambda', \hat{s} \eta, \hat{s} \eta'}^s \\ &\quad V_{\mathbf{Q}_{\eta\eta'}, \hat{s}, n}^s(\omega) M_{F\Lambda', \hat{s} \eta, \hat{s} \eta', \sigma}^{s\dagger}(\bar{\omega}) c_{\Lambda' \hat{s} \eta' \sigma} | 0_{\Lambda \hat{s} \eta \sigma} 1_{\Lambda' \hat{s} \eta' \sigma} \rangle \quad (45) \end{aligned}$$

where the green function $\hat{G}_{F, \Lambda, \Lambda', \hat{s} \eta, \hat{s} \eta'}^{c, s}$ for the doublon-holon/two spinon pseudospin coupled to fermion is written in the basis $\mathcal{B} = \{|\Psi_{F\Lambda \hat{s} \eta \hat{s} \eta' - \sigma}\rangle, |\Psi_{F\Lambda \hat{s} \eta \hat{s} \eta' - \sigma}^\perp\rangle\}$

$$\begin{aligned} |\Psi_{F\Lambda \hat{s} \eta \hat{s} \eta' - \sigma}\rangle &= \sqrt{p_c} |\uparrow_{F\hat{s} \eta}^c 0_{-\Lambda T \hat{s} \eta' - \sigma} 0_{-\Lambda' T \hat{s} \eta' - \sigma}\rangle + \sqrt{p_s} |\uparrow_{F\hat{s} \eta}^s 0_{-\Lambda T \hat{s} \eta' - \sigma} 0_{-\Lambda' T \hat{s} \eta' - \sigma}\rangle, \\ |\Psi_{F\Lambda \hat{s} \eta \hat{s} \eta' - \sigma}^\perp\rangle &= \sqrt{p_c} |\downarrow_{F\hat{s} \eta}^c 0_{-\Lambda T \hat{s} \eta' - \sigma} 0_{-\Lambda' T \hat{s} \eta' - \sigma}\rangle + \sqrt{p_s} |\downarrow_{F\hat{s} \eta}^s 0_{-\Lambda T \hat{s} \eta' - \sigma} 0_{-\Lambda' T \hat{s} \eta' - \sigma}\rangle \quad (46) \end{aligned}$$

given by ,

$$\begin{aligned} &\hat{G}_{F, \Lambda, \Lambda', \hat{s} \eta, \hat{s} \eta'}^{c, s}(\bar{\omega}) \\ &= p_c |\uparrow_{F\hat{s} \eta}^c 0_{-\Lambda T \hat{s} \eta' - \sigma} 0_{-\Lambda' T \hat{s} \eta' - \sigma}\rangle \left(\bar{\omega} + \epsilon_{-\Lambda T \hat{s}} + \epsilon_{-\Lambda' T \hat{s}} - \frac{V_{\mathbf{Q}_{\eta\eta'}, \hat{s}, n}^c(\omega)}{4} \right)^{-1} \langle \uparrow_{F\hat{s} \eta}^c 0_{-\Lambda T \hat{s} \eta' - \sigma} 0_{-\Lambda' T \hat{s} \eta' - \sigma} | \\ &+ p_s |\downarrow_{F\hat{s} \eta}^s 1_{-\Lambda T \hat{s} \eta' - \sigma} 1_{-\Lambda' T \hat{s} \eta' - \sigma}\rangle \left(\bar{\omega} - \epsilon_{-\Lambda T \hat{s}} - \epsilon_{-\Lambda' T \hat{s}} - \frac{V_{\mathbf{Q}_{\eta\eta'}, \hat{s}, n}^s(\omega)}{4} \right)^{-1} \langle \downarrow_{F\hat{s} \eta}^s 1_{-\Lambda T \hat{s} \eta' - \sigma} 1_{-\Lambda' T \hat{s} \eta' - \sigma} |. \quad (47) \end{aligned}$$

The integrals $I_{\Lambda\hat{s}}$ in eq(45) can be computed in the following way,

$$\begin{aligned}
I_{\Lambda\hat{s}} &= \int d\bar{\omega} d\Lambda' \langle 0_{\Lambda\hat{s}\eta\sigma} 1_{\Lambda'\hat{s}\eta'\sigma} | V_{\mathbf{Q}\eta\eta',\hat{s},n}^c(\omega) c_{\Lambda\hat{s}\eta\sigma}^\dagger M_{F\Lambda,\hat{s}\eta,\hat{s}\eta',\sigma}^c(\bar{\omega}) G_{F,\Lambda,\Lambda',\hat{s}\eta,\hat{s}\eta'}^c \\
&\quad V_{\mathbf{Q}\eta\eta',\hat{s},n}^c(\omega) M_{F\Lambda',\hat{s}\eta,\hat{s}\eta',\sigma}^{c\dagger}(\bar{\omega}) c_{\Lambda'\hat{s}\eta'\sigma} | 0_{\Lambda\hat{s}\eta\sigma} 1_{\Lambda'\hat{s}\eta'\sigma} \rangle \\
&= \frac{1}{W} \int_{-\frac{W}{2}}^{\frac{W}{2}} d\bar{\omega} \int_{-\Lambda_n}^{\Lambda_n} d\Lambda' \frac{(V_{\mathbf{Q}\eta\eta',\hat{s},n}^c(\omega))^2}{\bar{\omega} + \epsilon_{-\Lambda T\hat{s}} + \epsilon_{-\Lambda' T\hat{s}} - \frac{V_{\mathbf{Q}\eta\eta',\hat{s},n}^c(\omega)}{4}} \\
&= 4V_{\mathbf{Q}\eta\eta',\hat{s},n}^c(\omega) \int_{\frac{W}{2} - \frac{V_{\mathbf{Q}\eta\eta',\hat{s},n}^c(\omega)}{4}}^{\frac{W}{2}} d\bar{\omega} \int_{-\Lambda_n}^{\Lambda_n} d\Lambda' \frac{1}{\bar{\omega} + \epsilon_{-\Lambda T\hat{s}} + \epsilon_{-\Lambda' T\hat{s}}} \\
&= 4V_{\mathbf{Q}\eta\eta',\hat{s},n}^c(\omega) \oint_{\frac{W}{2} - \frac{V_{\mathbf{Q}\eta\eta',\hat{s},n}^c(\omega)}{4}}^{\frac{W}{2}} dz \int_{-\Lambda_n}^0 d\Lambda' \frac{1}{z + \epsilon_{-\Lambda T\hat{s}} + \epsilon_{-\Lambda' T\hat{s}}} \\
&= 2p_c V_{\mathbf{Q}\eta\eta',\hat{s},n}^c(\omega) \frac{\Lambda_{n,\omega}^c(\hat{s})}{\Lambda_0} (sgn(e^{i\gamma_{\hat{s},\mathbf{Q}\eta\eta'}(\omega)}) + 1) \theta(\Lambda_{n,\omega}^c(\hat{s}) - \Lambda) ,
\end{aligned}$$

where $\gamma_{\hat{s},\mathbf{Q}\eta\eta'=(0,\pi)}(\omega) = \gamma_{\hat{s},(\uparrow,\downarrow)}(\omega)$, (48)

where $\frac{\Lambda_{n,\omega}^c(\hat{s})}{\Lambda_0}$ is the geometric measure of the number of poles for the doublon-holon collective entities, similarly for the two spinon scattering processes the imaginary part of the self would have had a contribution $p_s V_{\mathbf{Q}\eta\eta',\hat{s},n}^s(\omega) \frac{\Lambda_{n,\omega}^s(\hat{s})}{\Lambda_0}$. An explanatory figure representing the virtual states being contour integrated over is shown in Fig.(16). With the computation of the following integrals leads to the imaginary self energy matrix,

$$\hat{\Sigma}_{\Lambda,\hat{s},n}^{Im}(\omega) = (c_{\Lambda\hat{s}\sigma}^\dagger c_{\Lambda-T\hat{s}\sigma}) \begin{pmatrix} 4V_{\mathbf{Q}=0,\hat{s},n}(\omega) N_{\mathbf{Q}=0,\hat{s}}(\omega) & 4V_{\mathbf{Q}=\pi,\hat{s},n}(\omega) N_{\mathbf{Q}=\pi,\hat{s}}(\omega) \\ 4V_{\mathbf{Q}=\pi,\hat{s},n}(\omega) N_{\mathbf{Q}=\pi,\hat{s}}(\omega) & 4V_{\mathbf{Q}=0,\hat{s},n}(\omega) N_{\mathbf{Q}=0,\hat{s}}(\omega) \end{pmatrix} \begin{pmatrix} c_{\Lambda\hat{s}\sigma} \\ c_{\Lambda-T\hat{s}\sigma}^\dagger \end{pmatrix} \quad (49)$$

where $N_{\mathbf{Q}\eta\eta',\hat{s}}(\omega) = (sgn(e^{i\gamma_{\hat{s},\mathbf{Q}\eta\eta'}(\omega)}) + 1)$ and

$$\begin{aligned}
V_{\mathbf{Q}=(0,\pi),\hat{s},n}(\omega) &= (p_c V_{\mathbf{Q}=(0,\pi),\hat{s},n}^c(\omega) \frac{\Lambda_{n,\omega}^c(\hat{s})}{\Lambda_0} \theta(\Lambda_{n,\omega}^c(\hat{s}) - \Lambda) \\
&\quad + p_s V_{\mathbf{Q}=(0,\pi),\hat{s},n}^s(\omega) \frac{\Lambda_{n,\omega}^s(\hat{s})}{\Lambda_0} \theta(\Lambda_{n,\omega}^s(\hat{s}) - \Lambda)) N_{\mathbf{Q}\eta\eta',\hat{s}}(\omega) .
\end{aligned} \quad (50)$$

At the final fixed point of the RG flow the self energy matrix has the following form,

$$\hat{\Sigma}_{\Lambda,\hat{s},n}^{Im}(\omega) = (c_{\Lambda\hat{s}\sigma}^\dagger c_{\Lambda-T\hat{s}\sigma}) \begin{pmatrix} 4V_{\mathbf{Q}=0,\hat{s},\Lambda_n^*}(\omega) N_{\mathbf{Q}=0,\hat{s}}(\omega) & 4V_{\mathbf{Q}=\pi,\hat{s},\Lambda_n^*}(\omega) N_{\mathbf{Q}=\pi,\hat{s}}(\omega) \\ 4V_{\mathbf{Q}=\pi,\hat{s},\Lambda_n^*}(\omega) N_{\mathbf{Q}=\pi,\hat{s}}(\omega) & 4V_{\mathbf{Q}=0,-T\hat{s},\Lambda_n^*}(\omega) N_{\mathbf{Q}=0,\hat{s}}(\omega) \end{pmatrix} \begin{pmatrix} c_{\Lambda\hat{s}\sigma} \\ c_{\Lambda-T\hat{s}\sigma}^\dagger \end{pmatrix} , \quad (51)$$

where the fixed point values of the coupling coefficients are given by,

$$\begin{aligned} V_{\mathbf{Q}=0, \hat{s}, n^*}(\omega) = V_{\mathbf{Q}=0, -T\hat{s}, n^*}(\omega) &= p_c \epsilon_{\Lambda_n^* \hat{s}}^c + p_s \epsilon_{\Lambda_n^* \hat{s}}^s + \frac{W}{2} - \omega \\ V_{\mathbf{Q}=\pi, \hat{s}, \Lambda_n^*}(\omega) &= \omega - p_c \epsilon_{\Lambda_n^* \hat{s}}^c - p_s \epsilon_{\Lambda_n^* \hat{s}}^s. \end{aligned} \quad (52)$$

Here $N_{\mathbf{Q}=\pi, \hat{s}}(\omega) + N_{\mathbf{Q}=0, \hat{s}}(\omega) = 1$, when $N_{\mathbf{Q}=\pi, \hat{s}}(\omega) = 1$ then the non-trivial topological number corresponds to gapping the electronic states due to backscattering, whereas when $N_{\mathbf{Q}=\pi, \hat{s}}(\omega) = 0$ then that corresponds to gapless electronic states undergoing forward scattering.

4.4 Computing the complete single particle green function from $\hat{\Sigma}^I$

The off-diagonal pieces of the self energy matrix generated due to Umklapp /spin backscattering process try to generate a gap for single electronic states by backscattering electronic states whereas the diagonal pieces generated from forward scattering determine the nature of poles for the gapless electronic states. This backscattering processes lead to a renormalized diagonal pieces. This renormalized pieces can be reached by decoupling the states along \hat{s} , $-\hat{s}$ while taking account of the motion flip backscattering or the backflow of the electrons,

$$\begin{aligned} \hat{\Sigma}_{\Lambda, \hat{s}, n}^{Im}(\omega) |\psi\rangle &= (\omega' - \omega) |\psi\rangle \\ \Sigma_{\Lambda, \hat{s}, n}^{Im++}(\omega) c_+ + \Sigma_{\Lambda, \hat{s}, n}^{Im+-}(\omega) c_- &= (\omega' - \omega) c_+ \\ \Sigma_{\Lambda, \hat{s}, n}^{Im-+}(\omega) c_+ + \Sigma_{\Lambda, \hat{s}, n}^{Im--}(\omega) c_- &= (\omega' - \omega) c_- \end{aligned} \quad (53)$$

Upon folding the off diagonal elements, we obtain

$$\begin{aligned} \left(\Sigma_{\Lambda, \hat{s}, n}^{Im++}(\omega) + \Sigma_{\Lambda, \hat{s}, n}^{Im+-}(\omega) \frac{1}{\omega' - \omega - \Sigma_{\Lambda, \hat{s}, n}^{Im--}(\omega)} \Sigma_{\Lambda, \hat{s}, n}^{Im-+}(\omega) \right) c_+ &= (\omega' - \omega) c_+ \\ \left(\Sigma_{\Lambda, \hat{s}, n}^{Im++}(\omega) + \Sigma_{\Lambda, \hat{s}, n}^{Im+-}(\omega) \frac{1}{\omega' - \omega - \Sigma_{\Lambda, \hat{s}, n}^{Im--}(\omega)} \Sigma_{\Lambda, \hat{s}, n}^{Im-+}(\omega) \right) c_- &= (\omega' - \omega) c_- . \end{aligned} \quad (54)$$

Therefore the renormalized self energy matrix is given by,

$$\begin{aligned} \hat{\Sigma}_{\Lambda, \hat{s}, n}^{Im}(\omega) &= (c_{\Lambda \hat{s} \sigma}^\dagger c_{\Lambda - T \hat{s} \sigma}) \\ &\begin{pmatrix} 4V_{\mathbf{Q}=0, \hat{s}, \Lambda_{n^*}}(\omega) N_{\mathbf{Q}=0, \hat{s}}(\omega) + 4V_{\mathbf{Q}=\pi, \hat{s}, \Lambda_{n^*}}(\omega) \frac{1}{\omega' - \omega - V_{\mathbf{Q}=0, \hat{s}, \Lambda_{n^*}}(\omega)} V_{\mathbf{Q}=\pi, \hat{s}, \Lambda_{n^*}}(\omega) N_{\mathbf{Q}=\pi, \hat{s}}(\omega) & 0 \\ 0 & (\hat{s} \rightarrow -T\hat{s}) \end{pmatrix} \\ &\begin{pmatrix} c_{\Lambda \hat{s} \sigma} \\ c_{\Lambda - T \hat{s} \sigma}^\dagger \end{pmatrix} \end{aligned} \quad (55)$$

The $Re(\Sigma)$ which can be in turn computed from the $Im(\Sigma)$ via the Kramers-Kronig relations,

$$\Sigma_{\Lambda, \hat{s}, n}^{Re} = \int_{-\infty}^{\infty} d\omega' \frac{4V_{\mathbf{Q}=0, \hat{s}, \Lambda_{n^*}}(\omega')}{\omega' - \omega} = 4V_{\mathbf{Q}=0, \hat{s}, \Lambda_{n^*}}(\omega) \ln \left(\frac{W}{W - 2\omega} \right) N_{\mathbf{Q}=0, \hat{s}}(\omega). \quad (56)$$

Now we can write the complete single particle green function $G_{n^* \sigma}(\Lambda, \hat{s}, \omega) = \langle c_{n^*, \Lambda \hat{s} \sigma}(\omega) c_{n^*, \Lambda \hat{s} \sigma}^\dagger(\omega) \rangle$,

$$\begin{aligned} G_{n^* \sigma}(\Lambda, \hat{s}, \omega) &= \frac{1}{\frac{W}{2} - \omega - \epsilon_{\Lambda \hat{s}} - \Sigma_{\Lambda, \hat{s}, n^*}^{Re}(\omega) - i \Sigma_{\Lambda, \hat{s}, n}^{Im}(\omega)} \\ &= \frac{Z_{\Lambda \hat{s}, n^*}(\omega)}{\frac{W}{2} - \omega - \epsilon_{\Lambda \hat{s}} - i \Sigma_{\Lambda, \hat{s}, n}^{Im}(\omega)} + \frac{1}{\omega - \epsilon_{\Lambda \hat{s}} - i \Sigma_{\Lambda, \hat{s}, n^*}^{Im}(\omega)} \left[\frac{1}{1 - \frac{\Sigma_{\Lambda, \hat{s}, n^*}^{Re}(\omega)}{\omega - \epsilon_{\Lambda \hat{s}} - i \Sigma_{\Lambda, \hat{s}, n^*}^{Im}(\omega)}} - Z_{\Lambda \hat{s}, n^*}^{-1}(\omega) \right] \end{aligned} \quad (57)$$

where $Z_{\Lambda \hat{s}, n^*}(\omega) = \left(1 - \frac{\partial \Sigma_{\Lambda, \hat{s}, n^*}^{Re}(\omega)}{\partial (\frac{W}{2} - \omega)} \right)^{-1}$ is the quasiparticle residue and the inverse lifetime of the single fermion quasiparticle is contained in the imaginary part of the self energy.

4.5 Pole to zero conversion in the single fermion propagator

At a given probe energy scale, there is continuous region with normal orientations \hat{s}' s ranging from the AN to \hat{s}_ω upto which $N_{\mathbf{Q}=0, \hat{s}}(\omega) = 1 - N_{\mathbf{Q}=\pi, \hat{s}}(\omega) = 0$. This topological signature leads to a pole of the imaginary part of self energy, and in turn a vanishing lifetime (and a zero of the Greens function G) [24]

$$\begin{aligned} N_{\mathbf{Q}=\pi, \hat{s}}(\omega) = 1 \rightarrow G_{n^* \sigma}(\Lambda, \hat{s}, \omega) &= \frac{1}{\frac{W}{2} - \omega - \epsilon_{\Lambda \hat{s}} - \Sigma_{\Lambda, \hat{s}, n^*}^{Re}(\omega) - i \frac{4V_{\mathbf{Q}=\pi, \hat{s}, \Lambda_{n^*}}^2(\omega)}{\omega' - \omega} \Big|_{\omega' \rightarrow \omega}} \\ &= \frac{1}{\frac{W}{2} - \omega - \epsilon_{\Lambda \hat{s}} - \Sigma_{\Lambda, \hat{s}, n^*}^{Re}(\omega) - i\infty} = 0. \end{aligned} \quad (58)$$

4.6 Decay in quasiparticle residue

The quasiparticle residue $Z_{\Lambda\hat{s},n^*}(\omega)$ computed from the real part of the self energy $\Sigma_{\Lambda\hat{s},n^*}^{Re}(\omega)$ can be shown to vanish logarithmically upon approaching the Fermi surface [28]

$$Z_{\Lambda\hat{s},n^*}(\omega) = 1 / \log \left(\frac{\varepsilon_{\Lambda_0}(\hat{s})}{\varepsilon_{\Lambda_n^*,\omega}(\hat{s})} \right) \rightarrow 0 \text{ as } \omega \rightarrow \frac{W}{2}. \quad (59)$$

5 f-sum rules preservation in gapped regions, spectral weight redistribution

The f-sum rule can be preserved in the gapped regions by addition of spectral weights from the single particle ($G_{\Lambda\hat{s},n^*}^{(1)}(\omega)$) and two particle green function ($G_{\Lambda\hat{s},n^*}^{(2)}(\omega)$) [55]

$$f_\pi(\omega) = \sum_{\Lambda\hat{s}} \int d\bar{\omega} [G_{\Lambda\hat{s},n^*}^{(1)}(\bar{\omega}) + G_{\Lambda\hat{s},n^*}^{(2)}(\bar{\omega})] \quad (60)$$

where ,

$$G_{\Lambda\hat{s},n^*}^{(1)}(\bar{\omega}) = \frac{1}{\bar{\omega} - \epsilon_{\Lambda\hat{s}} - \Sigma_{\Lambda\hat{s},n^*}^{Re}(\omega) - i \frac{4V_{\mathbf{Q}=\pi,\hat{s},\Lambda_n^*}^2(\omega)}{\omega' - \omega} \Big|_{\omega' \rightarrow \omega}}, \quad (61)$$

and,

$$G_{\Lambda\hat{s},n^*}^{(2)}(\bar{\omega}) = \frac{1}{\bar{\omega} - \epsilon_{\Lambda\hat{s}}^{tot} - (\omega - \epsilon_{\Lambda^*\hat{s}}^{tot})N_{\mathbf{Q}=\pi,\hat{s}}(\bar{\omega}) - i \frac{\epsilon_{\Lambda\hat{s}}^{tot2}}{4V_{\mathbf{Q}=\pi,\hat{s},\Lambda_n^*}(\bar{\omega})N_{\mathbf{Q}=\pi,\hat{s}}(\omega)}}, \quad (62)$$

with $\epsilon_{\Lambda\hat{s}}^{tot} = p_c \epsilon_{\Lambda\hat{s}}^c + p^s \epsilon_{\Lambda\hat{s}}^s$. In the gapped regions where $N_{\mathbf{Q}=\pi,\hat{s}}(\bar{\omega}) = 1$, the two particle green function can be written as

$$\begin{aligned} G_{\Lambda\hat{s},n^*}^{(2)}(\bar{\omega}) &= \frac{1}{\bar{\omega} - \epsilon_{\Lambda\hat{s}}^{tot} - \omega + \epsilon_{\Lambda^*\hat{s}}^{tot}}, \\ \frac{\partial [G_{\Lambda\hat{s},n^*}^{(2)}(\bar{\omega})]^{-1}}{\partial \bar{\omega}} &= 1 \rightarrow G_{\Lambda\hat{s},n^*}^{(2)}(\bar{\omega}) \partial_\omega \frac{\partial [G_{\Lambda\hat{s},n^*}^{(2)}(\bar{\omega})]^{-1}}{\partial \bar{\omega}} = G_{\Lambda\hat{s},n^*}^{(2)}(\bar{\omega}) \end{aligned} \quad (63)$$

using this the f sum rule for the gapped regions can be represented as,

$$\begin{aligned}
f_\pi(\omega) &= \nu \frac{\sum_{\hat{s}} N_{\mathbf{Q}=\pi, \hat{s}}(\omega)}{\sum_{\hat{s}} 1} = \sum_{\Lambda \hat{s}} \int d\bar{\omega} \left[G_{\Lambda, \hat{s}, n^*}^{(2)}(\bar{\omega}) \partial_{\bar{\omega}} \frac{\partial [G^{(2)}_{\Lambda, \hat{s}, n^*}(\bar{\omega})]^{-1}}{\partial \bar{\omega}} + G_{\Lambda, \hat{s}, n^*}^{(1)}(\bar{\omega}) \right], \\
&= \sum_{\Lambda \hat{s}} \int d\bar{\omega} \left[G_{\Lambda, \hat{s}, n^*}^{(2)}(\bar{\omega}) \partial_{\bar{\omega}} \frac{\partial [G^{(2)}_{\Lambda, \hat{s}, n^*}(\bar{\omega})]^{-1}}{\partial \bar{\omega}} + G_{\Lambda, \hat{s}, n^*}^{(1)}(\bar{\omega}) \right] \\
&= \sum_{\Lambda \hat{s}} \int d\bar{\omega} \left[\ln G_{\Lambda, \hat{s}, n^*}^{(2)}(\bar{\omega}) + G_{\Lambda, \hat{s}, n^*}^{(1)}(\bar{\omega}) \right] \\
&= \sum_{\Lambda \hat{s}} \left[\underbrace{1 \times \theta^{(2)}(\Lambda_{n^*, \hat{s}} - \Lambda)}_{\text{poles of } G^{(2)}} + \underbrace{0 \times \theta^{(1)}(\Lambda_{n^*, \hat{s}} - \Lambda)}_{\text{zeros of } G^{(1)}} + 1 \times \theta^{(1)}(\Lambda - \Lambda_{n^*, \hat{s}}) \right] \quad (64)
\end{aligned}$$

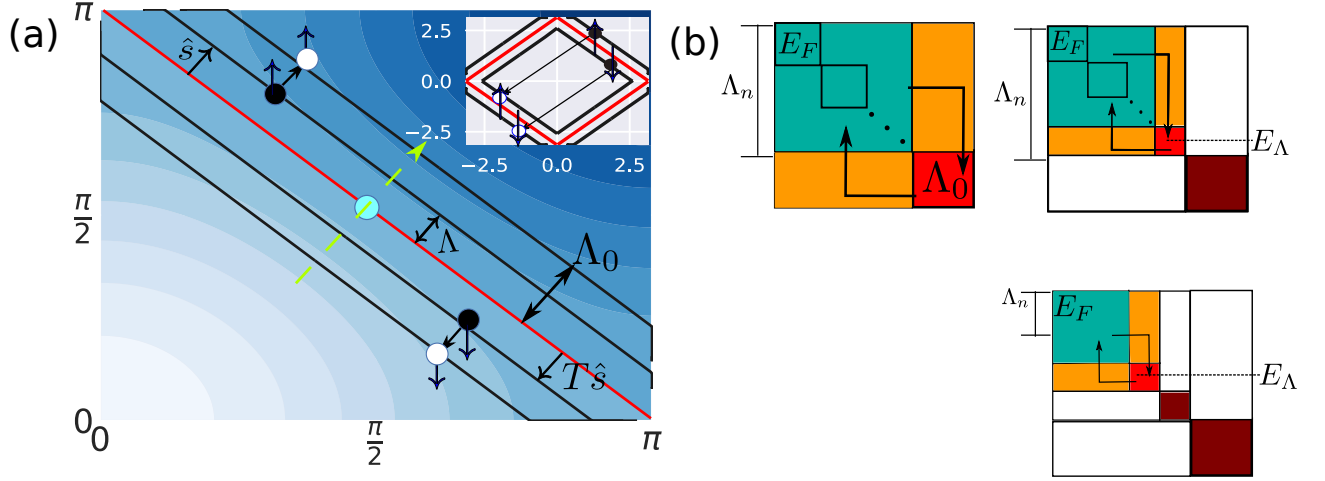


Fig. S1. (a) Construction of shells around the Fermi surface with a pair of black and white dots showing the up, down orientation of the pseudospin formed around the nodal point (cyan dot). The nodal vector (π, π) is indicated by the lime green arrow, and \hat{s} represents the normal vectors to the Fermi surface at every point on the shell. The inset in Fig(a) shows backscattering of the pseudospin electron pair, while the main figure shows a forward scattering event. (b) Recursive Gauss-Jordan diagonalisation of the many-body state space (in the two-particle pseudospin basis) by folding the pivot (red box) interpolating between the high-energy (brown box) and low-energy sector (green box). Orange boxes indicate connectivities between the pivot and low-energy sector.

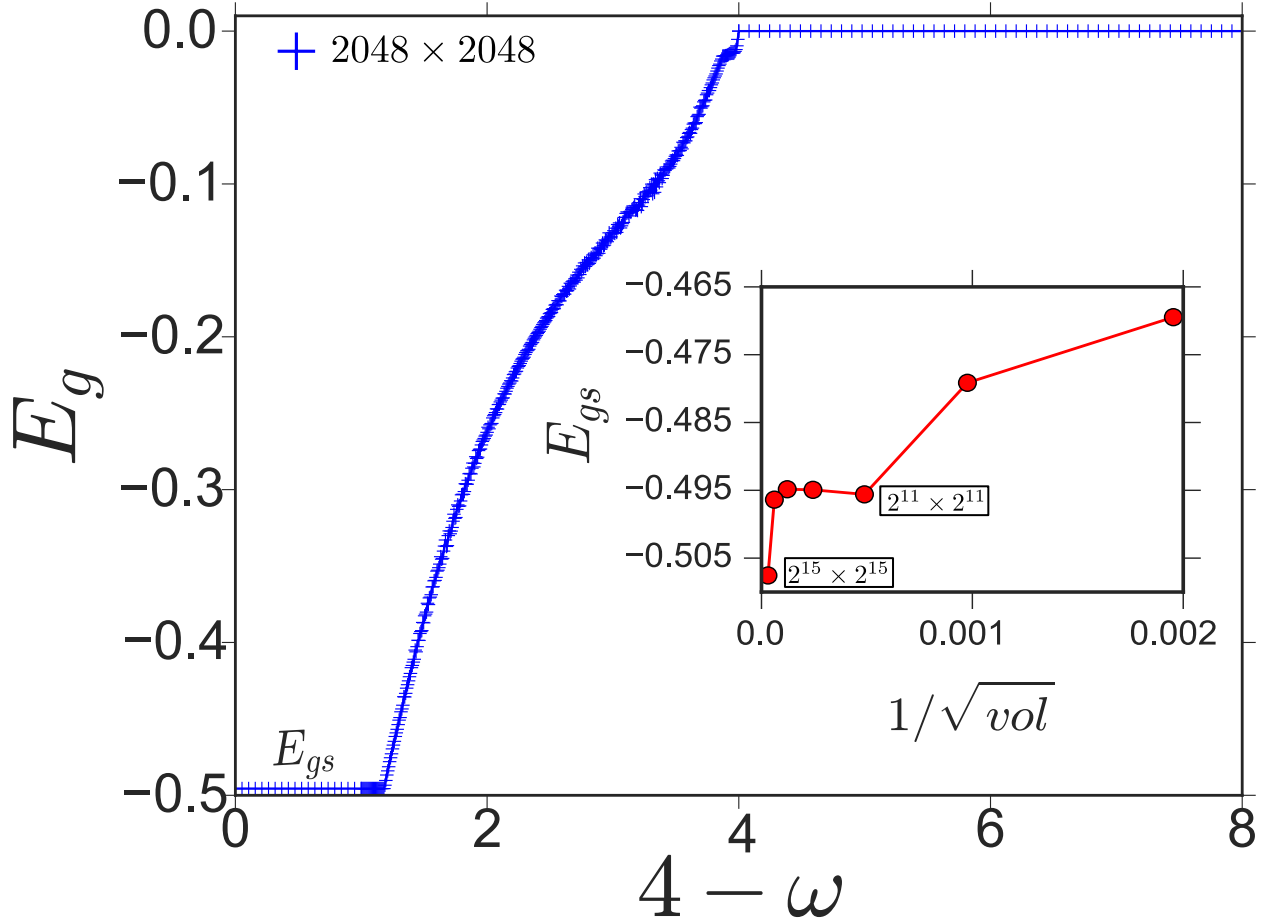


Fig. S2. Variation of ground state energy per particle (E_g) with the probe energy scale ω at half-filling and $U = 8t$ during the passage from metal ($\omega < 0$) to the Mott liquid ($\omega > 2.8$) through the pseudogap ($0 \leq \omega \leq 2.8$). A saturation value of $E_g = -0.495t$ for a k -space grid of $2^{11} \times 2^{11}$ (and $t = 1$). Inset: Finite-size scaling of the saturation value for $E_g \equiv E_{gs}$ with $1/\sqrt{\text{Volume}}$ with increasing k -space grid size from $2^9 \times 2^9$ to $2^{15} \times 2^{15}$. The saturation E_{gs} for the largest grid is observed to be $-0.507t$. The error bar for all data points is $\sim O(10^{-5}t)$.

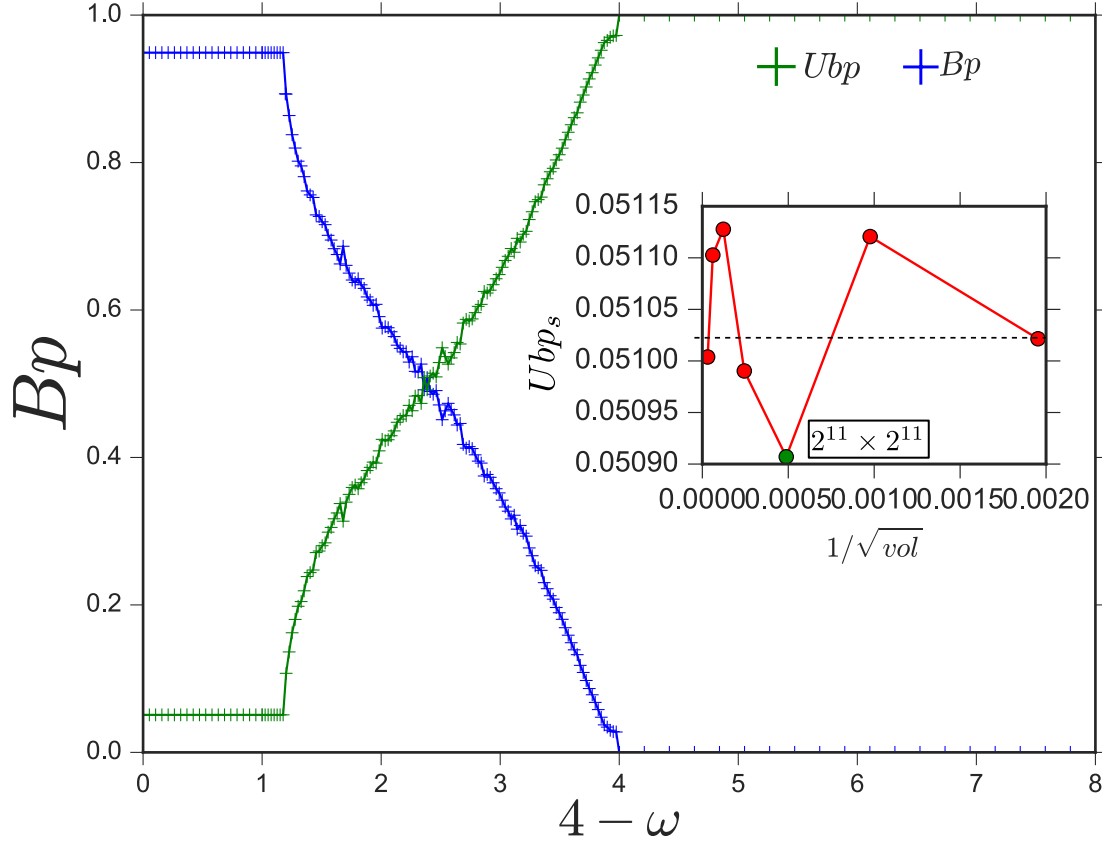


Fig. S3. Blue curve: Growth in fraction of bound pairs (Bp) of electronic states (holon-doublon/two-spinon) within the low-energy window at half-filling and $U = 8t$ during the passage from metal ($\omega < 0$) to the Mott liquid ($\omega > 2.8$) through the pseudogap ($0 \leq \omega \leq 2.8$). Green curve: Concomitant decay in fraction of unbound pairs (Ubp). Calculations are done for a k -space grid of $2^{11} \times 2^{11}$. Inset: Finite-size scaling of the saturation value for the fraction of unbound pairs in the Mott liquid with $1/\sqrt{\text{Volume}}$ with increasing k -space grid size from $2^9 \times 2^9$ to $2^{15} \times 2^{15}$. The saturation fraction display small fluctuations about an average value ~ 0.051 . Green point is the k -space grid used in the main figure. The error bar for all data points is $\sim O(10^{-5})$.

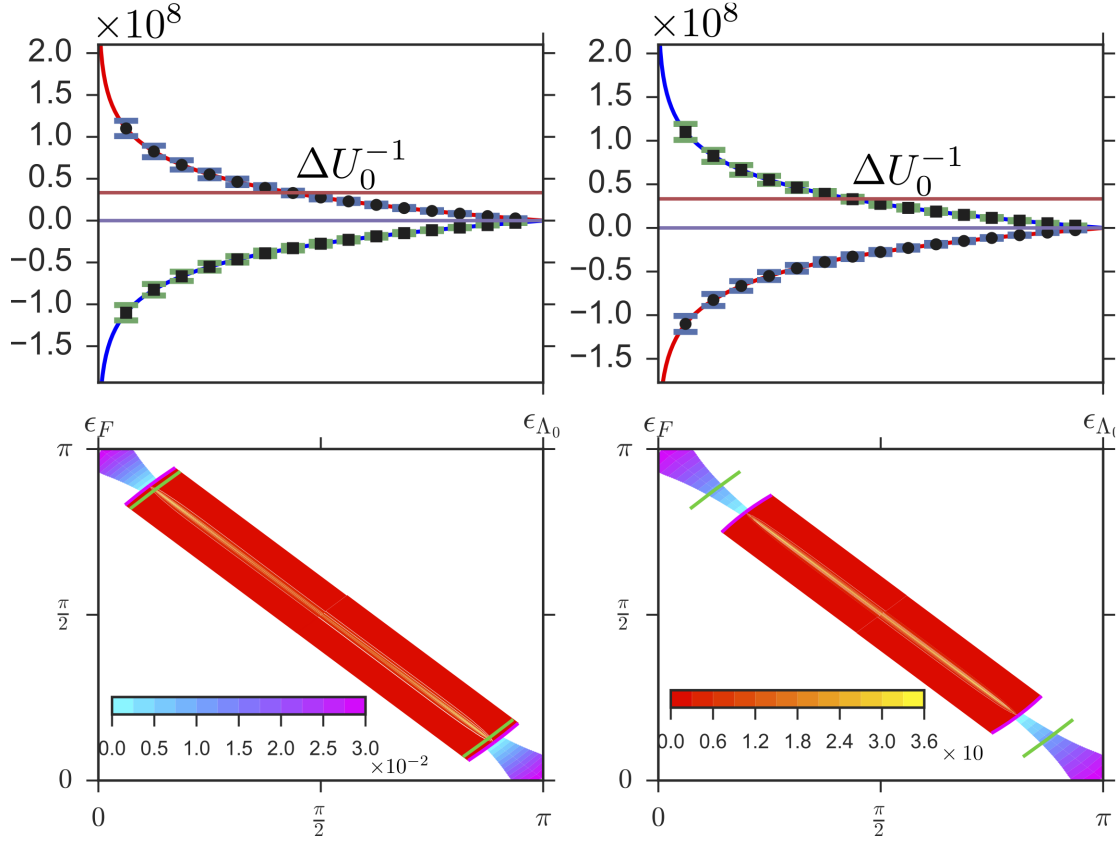


Fig. S4. (a) Pole of the of the two-particle (doublon-holon) gapless collective excitation (left panel)/ bound-state (right panel) is observed at a given point on the Fermi surface through a crossing of its phase Φ_{FS}/Φ_{BS} (red/blue line) with the energy scale for quantum fluctuations associated with the inverse bare interaction strength ΔU_0^{-1} . (b) From left to right: the gradual loss of spectral weight for the marginal electronic quasiparticle (red region) around the Fermi surface (thin yellow line) as the gapped bound pairs of doublons and holons (violet-blue regions) progress from the antinodes towards the nodes. The thin cyan line shows the change of a given state at the Fermi surface from a pole of the single-particle Greens function to that of the doublon-holon backscattering Greens function.

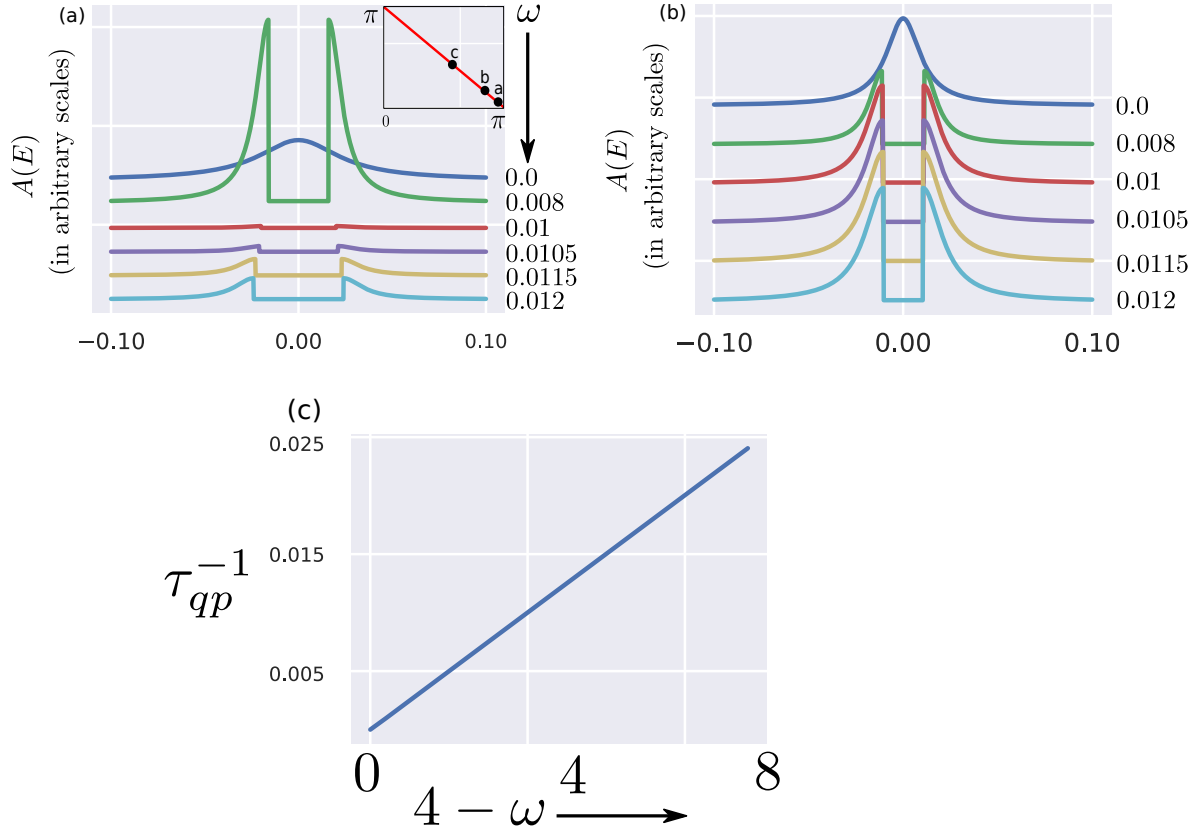


Fig. S5. (a) and (b) are the spectral functions $A(E)$ as a function of the probe energy E at and near the antinode (shown as points **a** and **b** in the inset of (a)) with varying quantum fluctuation energy $4 - \omega$. (a) shows a very drastic and abrupt transfer of spectral weight at the antinodes from a non-Fermi liquid metal to a progressively growing pseudogap as $4 - \omega$ is lowered. The pseudogapping near the antinode (point **b** in inset of (a)) is, however, gradual in nature. (c) The inverse lifetime of the electronic quasiparticles (i.e., the width of the spectral function curves at the nodal point (point **c** in inset of (a))) shows linear variation with $4 - \omega$, indicating non-Fermi liquid character (marginal Fermi liquid).

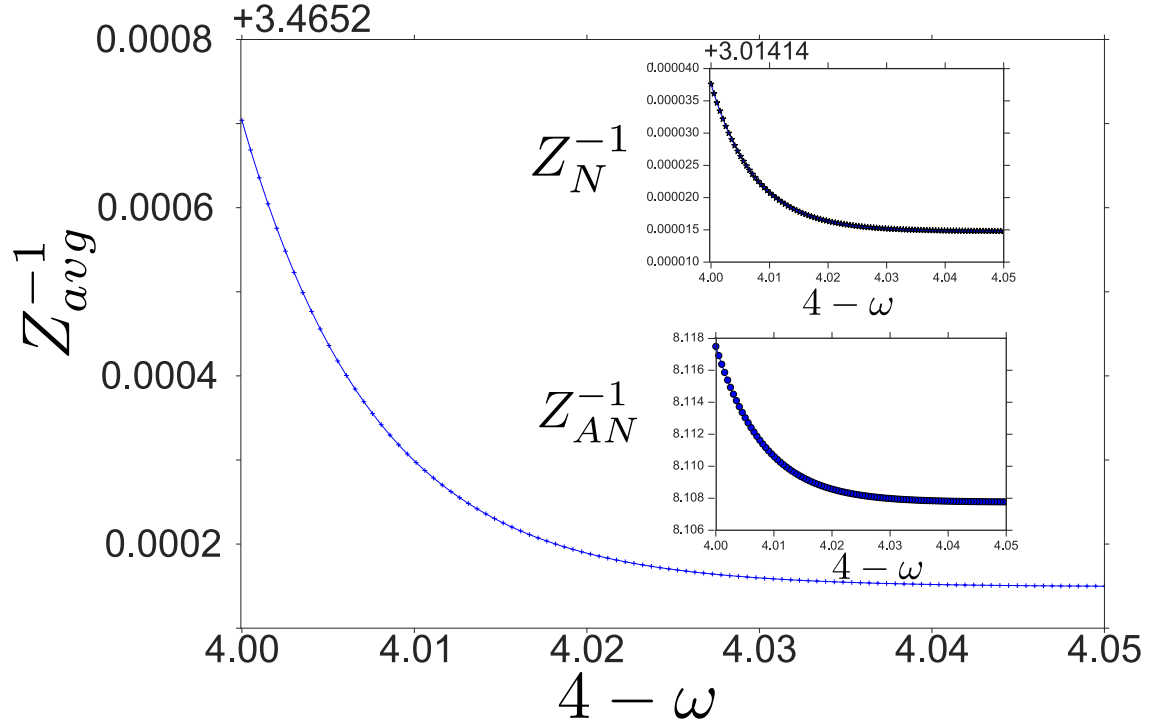


Fig. S6. Inverse quasiparticle residue averaged over a gapless connected Fermi surface Z_{avg}^{-1} at energies above the entry into the pseudogap phase shows a logarithmic growth as $4 - \omega$ is lowered. Such a vanishing of quasiparticle residue is an important characteristic of a marginal Fermi liquid. Insets: Z^{-1} at the node (top panel) and at the antinode (bottom panel) indicate existence of a non-Fermi liquid everywhere on a gapless connected Fermi surface, with a stronger spectral weight towards the antinodes.

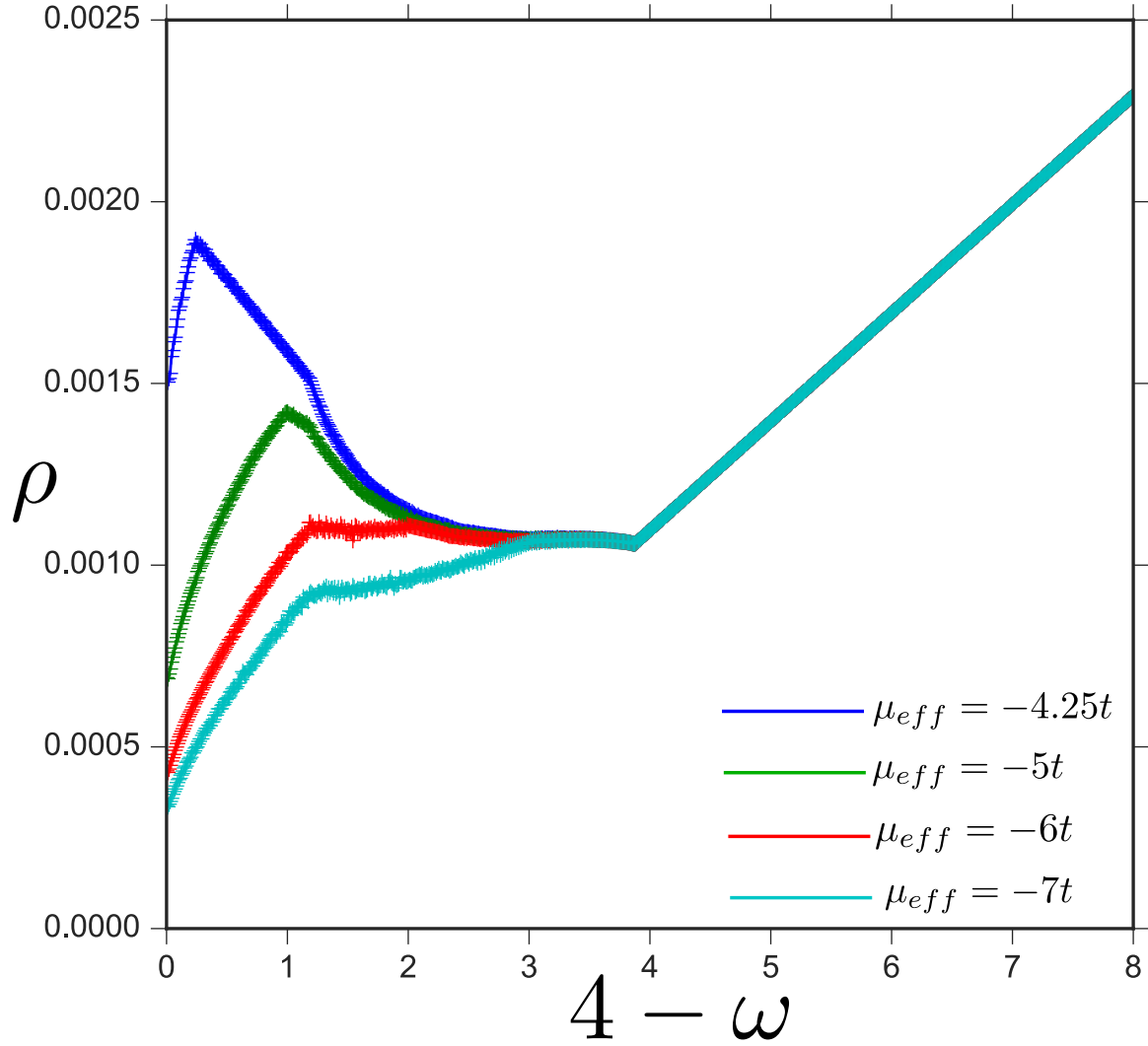


Fig. S7. Crossover in the resistivity (ρ) from a non-Fermi liquid metal at high-energies (linear against $4 - \omega$ upto $\omega \leq 0$) to a correlated Fermi liquid (CFL, $\omega \geq 2.5t$) at various doping strengths μ_{eff} greater than critical doping $\mu_{eff} = -4t$. The effects of a spin pseudogap at intervening energies is observed to be strong close to critical doping (blue and green curves) and weaken for larger dopings (red and cyan curves).

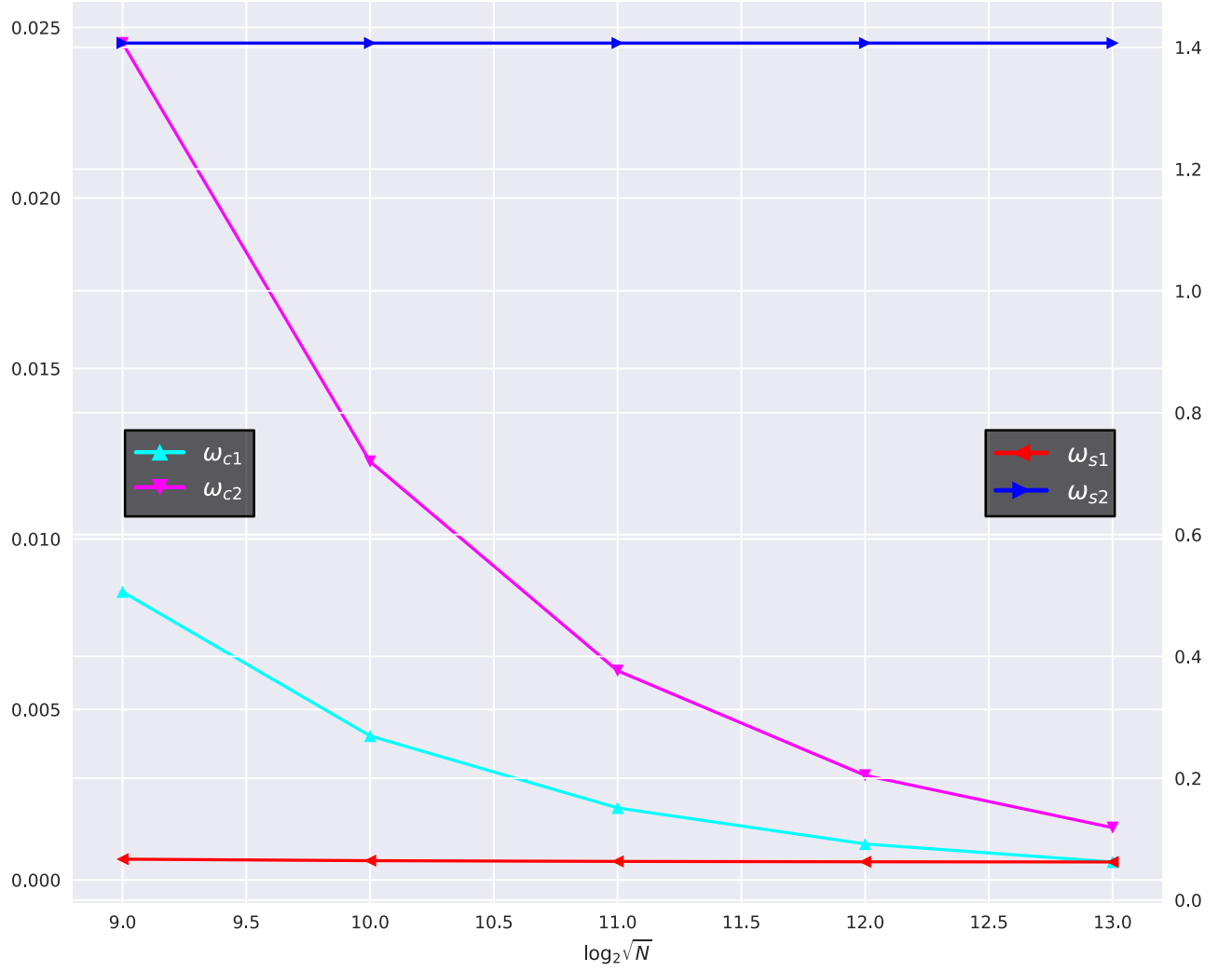


Fig. S8. Finite size scaling for the extent of the pseudogap. Cyan/red lines are the entry energy scales of the charge/spin pseudogap (ω_{c1}/ω_{s1}) respectively, while violet/blue lines are the exit energy scales (ω_{c2}/ω_{s2}) for the same. The vertical axis on the left corresponds to energies for charge excitations, while the right corresponds to energies for spin excitations.

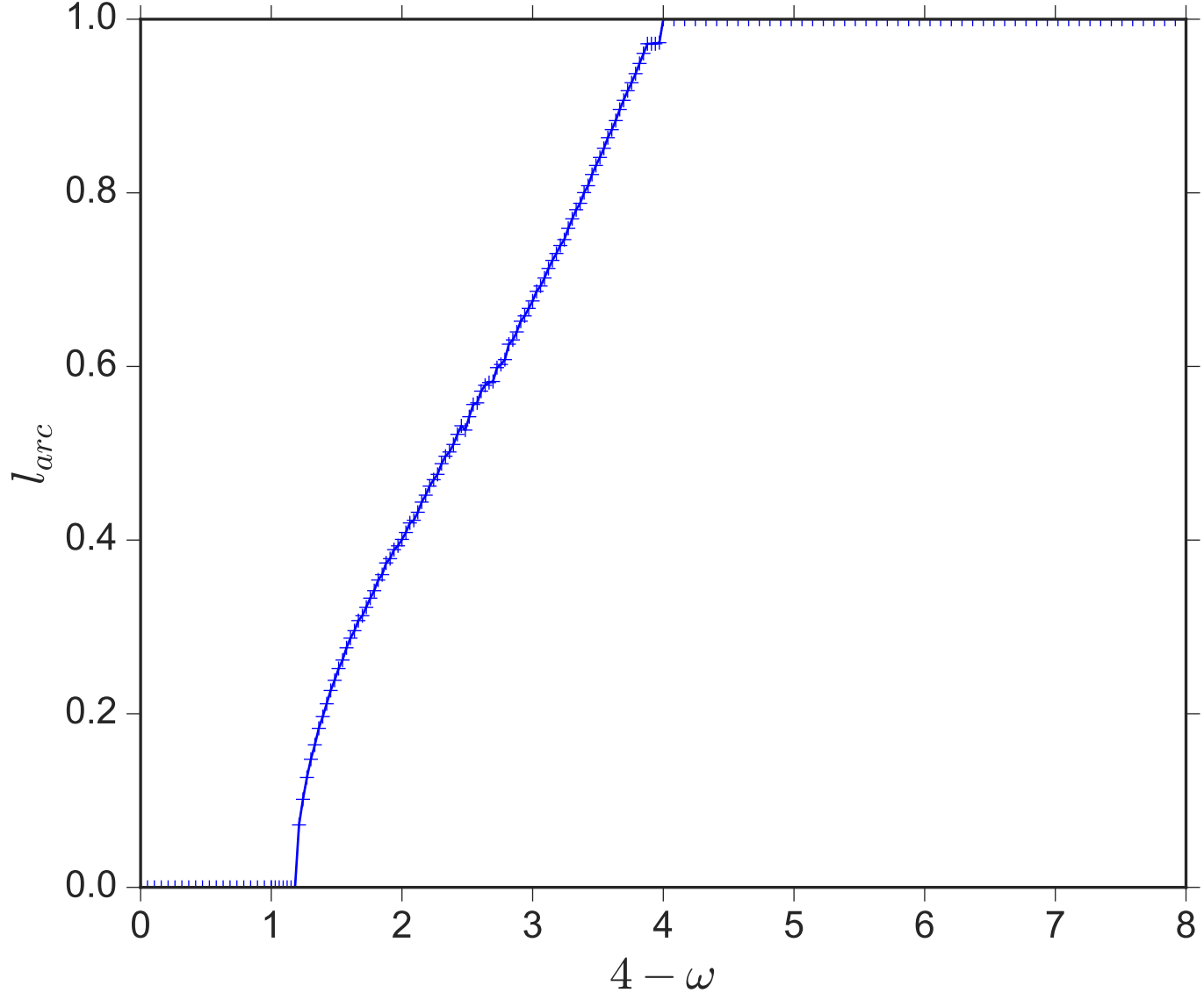


Fig. S9. Gradually decreasing Fermi arc length through the extent of the pseudogap with lowering quantum energy scale (increasing ω), leading to a Mott liquid with a completely gapped Fermi surface.

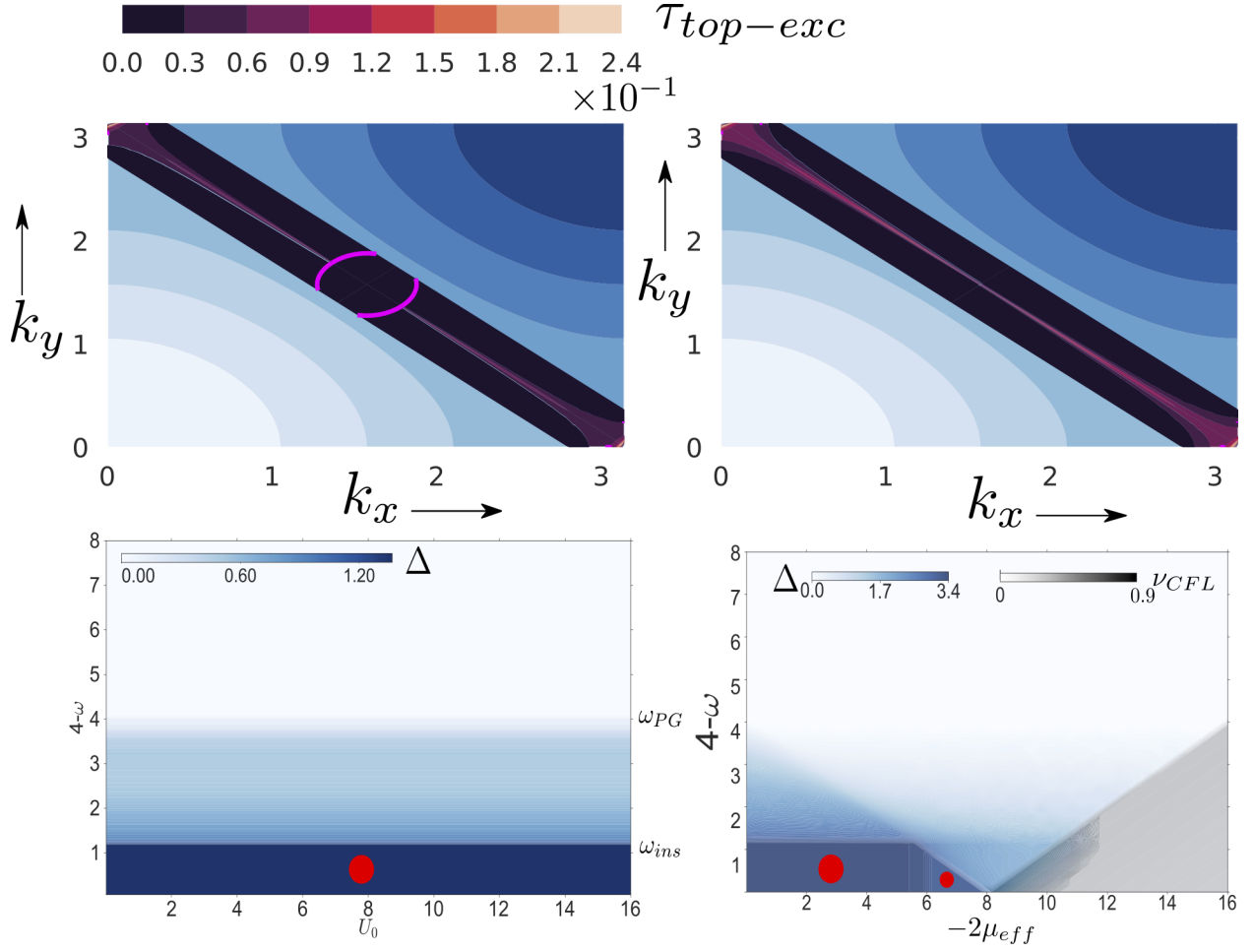


Fig. S10. Spectral weight for fractionally charged topological excitations of the charge sector in the low-energy neighbourhood of the Fermi surface (black rectangle) represented through the colorbar (black to light orange) in the pseudogap phase ((a), left panel), and in the Mott liquid ((a), right panel). The pink curves separate the gapless Fermi arcs from the gapped regions within the pseudogapped phase. The topological excitations form a connected surface (centered around the erstwhile Fermi surface) in the gapped Mott liquid phase. (b) The RG phase diagrams at (left panel), and away from (right panel), half-filling show the topologically ordered gapped Mott liquid phases through the red circles.

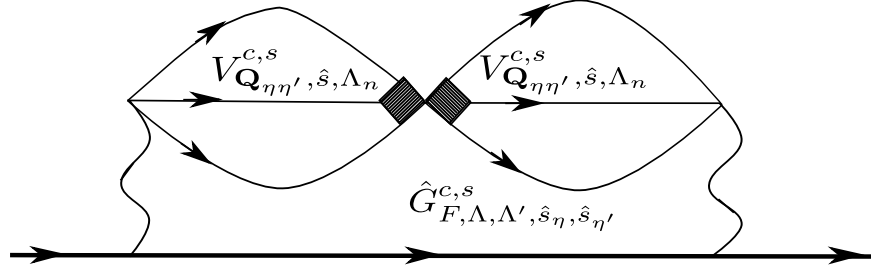


Fig. S11. Feynman diagram representing the renormalization of the single-particle self energy. The wiggly lines show virtual processes involving the intermediate virtual states of two electron-one hole *or* two hole-one electron. The solid lines shows the single electron Green function. The shaded squares shows the complete two-particle vertex for the forward and backward scattering process for doublon-holon or two-spinon pairs.

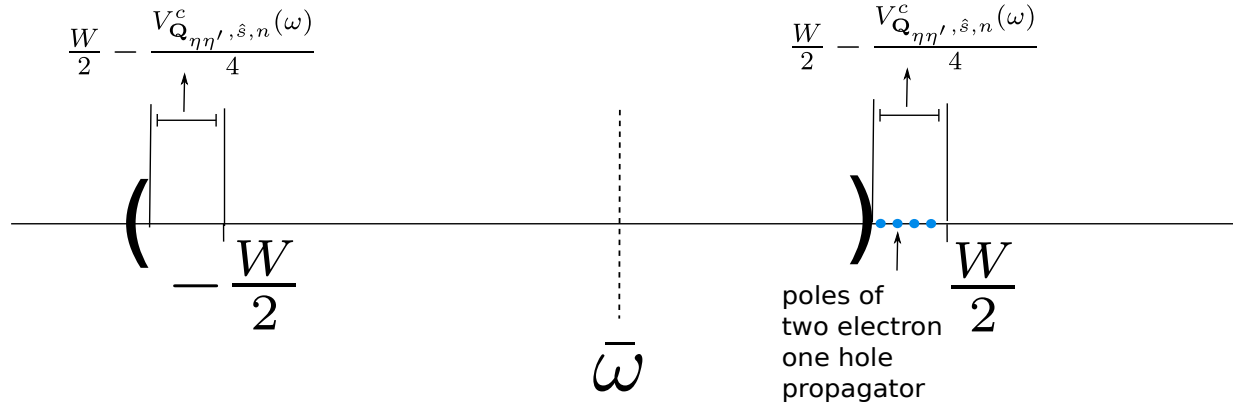


Fig. S12. Poles of the two electron-one hole intermediate virtual state that are countour integrated over in reaching the renormalised single-particle Greens function. $V_{\mathbf{Q}_{\eta\eta'},\hat{s},n}^c(\omega)$ represents the complete doublon-holon forward/backward scattering vertex, $\bar{\omega} = W/2 - \omega$ represents the scale for prob energy/quantum fluctuations.